Sustainable Cities and Society

Integrated impacts of cool coatings, street orientations, and height variability on urban cooling in 3D high-rise building arrays: CFD simulation

--Manuscript Draft--

Manuscript Number:	SCSI-D-25-10126R1
Article Type:	Full Length Article
Keywords:	cool coating; Urban morphology; Urban heat island (UHI); Computational Fluid Dynamics (CFD); Cooling strategy
Corresponding Author:	Lan Chen, PhD The Hong Kong Polytechnic University HONG KONG
First Author:	Tianyi Guan, PhD candidate
Order of Authors:	Tianyi Guan, PhD candidate
	Jian Hang, PhD
	Qingman Li, PhD candidate
	Lan Chen, PhD
	Guanwen Chen, PhD
	Hanying Dong, PhD
	Zhiwen Luo, PhD
Abstract:	Using cool coatings on building envelopes and modifying urban morphologies, such as street orientations and building height variability, are recognized as effective urban cooling strategies. However, few studies evaluate the integrated cooling performance of these strategies in three-dimensional (3D) high-rise building arrays. Moreover, most existing performance evaluations of cool coatings focus on temperature drop, while rarely considering coating costs. As a novel contribution, this study systematically investigates the combined impacts of cool coatings (cool roofs (CR), cool roofs & walls (CR&W), cool roofs & east-west walls (CR&EWW), and cool roofs & high-rise walls (CR&HW)), street orientations (north-south vs. east-west), and building height layouts (uniform-height vs. varied-height) on building surface temperature and pedestrian-level microclimate under three summer solar heating conditions (8 am, 12 pm, and 4 pm) using computational fluid dynamics simulations. Uniquely, cooling intensity (°C/m2) is proposed to quantify the average surface temperature drop per unit of cool-coated surface area by incorporating coating costs into cooling performance evaluation. Results indicate that cool coatings reduce direct sunlit surface temperatures by up to 7.5 °C, with ensemble-average building envelope drops of 0.36–1.63 °C, while their impacts on pedestrian-level air temperature (drop < 0.3 °C) and wind velocity ratio (variation < 0.06) are minimal. CR&W, CR&EWW, and CR&HW cause significantly greater ensemble-average temperature drops than CR; however, when coating costs are considered, CR&W is less cost-effective than other configurations. CR&EWW and CR&HW offer a good trade-off between cooling effect and coating costs. Moreover, north-south orientation generally shows superior cooling performance with cool coatings over east-west orientation. Height variability differentially influences the cool coating performance for high-rise and low-rise buildings. This study offers valuable insights for optimizing the spatial deployment of cool coatings in compact subtropical cities.
Response to Reviewers:	

Highlights

- Four coating combinations of cool roof and cool wall are compared.
- A novel index is proposed to include coating cost to assess cool coating efficacy.
- Adding cool wall to cool roof enhances the ensemble-average temperature drop.
- CR&EWW and CR&HW are a good trade-off between cooling effect and coating cost.
- Street orientation and height variability affect cool coating efficacy.

To be submitted to Sustainable Cities and Society 2025

Integrated impacts of cool coatings, street orientations, and height variability on urban cooling in 3D high-rise building arrays: CFD simulation

Abstract

Using cool coatings on building envelopes and modifying urban morphologies, such as street orientations and building height variability, are recognized as effective urban cooling strategies. However, few studies evaluate the integrated cooling performance of these strategies in three-dimensional (3D) high-rise building arrays. Moreover, most existing performance evaluations of cool coatings focus on temperature drop, while rarely considering coating costs. As a novel contribution, this study systematically investigates the combined impacts of cool coatings (cool roofs (CR), cool roofs & walls (CR&W), cool roofs & east-west walls (CR&EWW), and cool roofs & high-rise walls (CR&HW)), street orientations (north-south vs. east-west), and building height layouts (uniform-height vs. varied-height) on building surface temperature and pedestrian-level microclimate under three summer solar heating conditions (8 am, 12 pm, and 4 pm) using computational fluid dynamics simulations. Uniquely, cooling intensity (°C/m^2) is proposed to quantify the average surface temperature drop per unit of cool-coated surface area by incorporating coating costs into cooling performance evaluation.

Results indicate that cool coatings reduce direct sunlit surface temperatures by up to 7.5 °C, with ensemble-average building envelope drops of 0.36–1.63 °C, while their impacts on pedestrian-level air temperature (drop < 0.3 °C) and wind velocity ratio (variation < 0.06) are minimal. CR&W, CR&EWW, and CR&HW cause significantly greater ensemble-average temperature drops than CR; however, when coating costs are considered, CR&W is less cost-effective than other configurations. CR&EWW and CR&HW offer a good trade-off between cooling effect and coating costs. Moreover, north-south orientation generally shows superior cooling performance with cool coatings over east-west orientation. Height variability differentially influences the cool coating performance for high-rise and low-rise buildings. This study offers valuable insights for optimizing the spatial deployment of cool coatings in compact subtropical cities.

Keywords

Cool coating; Urban morphology; Urban heat island (UHI); Computational Fluid Dynamics (CFD); Cooling strategy

Nomenclature

A	Area of the mesh cell (m^2)
A_{cc}	Ensemble area of cool-coated building surfaces (m^2)
b	Counters of B
B	Number of target buildings per case, B = 9
CC	Cool coating
CFD	Computational Fluid Dynamics
CI	Cooling intensity (°C/m^2)
CM	Cooling magnitude (°C)

c_p	Specific heat ($J{\cdot}kg^{-1}{\cdot}K^{-1}$)
CR	Cool roofs
CR&EWW	Cool roofs and east-west walls
CR&HW	Cool roofs and high-rise walls
CR&W	Cool roofs and walls
DO	Discrete ordinate
E-W, EW	East-west
F_s	Safety factor, F_s = 1.25
g	Acceleration of gravity (m/s^2)
GCI	Grid convergence index
GCI_U, GCI_T	Grid convergence index of normalized wind velocity and air temperature
GMT	Greenwich Mean Time
H	Building height (m)
H_1	Height of low-rise building (m), H_1 = 36 m
H_2	Height of high-rise building (m), H_2 = 48 m
H_{max}	Maximum building height (m), H_{max} = 48 m
i, j	Directions of Cartesian coordinates
k	Turbulent kinetic energy (m^2/s^2)
L	Building length (m)
LT	Local time
NCC	No cool coating
N-S, NS	North-south
p	Pressure (Pa)
p_a	Formal order of accuracy
P_b	Turbulence production term due to buoyancy
P_k	Turbulence production term due to mean velocity gradients
q_r	Radiative heat flux (W/m^2)
Q_T	Heat production rate (W)
r	Linear grid refinement factor, $r = \sqrt{2}$
RANS	Reynolds-Averaged Navier-Stokes
Re	Reynolds number
S2S	Surface-to-surface
SIMPLE	Semi-Implicit Method for Pressure-Linked Equations
SOMUCH	Scaled Outdoor Measurement of Urban Climate and Health
t	Counters of TM
T, T_{air}	Air temperature (°C)
TM	Simulated local times in a given urban morphology and coating configuration, TM = 3
T_{sur}	Building surface temperature (°C)
U	Wind velocity (m/s)
U^*_{ABL}	Friction velocity of the atmospheric boundary layer (m/s)
UH	Uniform-height

UHI	Urban heat island
u_i, u_j	Velocity components in the directions of i and j (m/s)
U_{ref}	Reference wind velocity, $U_{ref} = 3$ m/s
VH	Varied-height
VR	Mean wind velocity normalized by the reference wind velocity
W	Building width (m)
w_1	Street width in the streamwise direction (m), $w_1 = 8$ m
w_2	Street width in the spanwise direction (m), $w_2 = 30$ m
$y+$	Non-dimensional distance
z_0	Roughness length (m)
z_{ref}	Reference height, $z_{ref} = 10$ m
β	Thermal expansion coefficient (K^{-1})
Γ_T	Effective thermal diffusivity (m^2/s)
δ_{ij}	Kronecker delta
ε	Turbulent dissipation rate (m^2/s^3)
κ	Von Karman constant, $\kappa = 0.41$
λ_p	Plan area index
μ	Kinetic viscosity (m^2/s)
μ_t	Turbulent eddy viscosity (m^2/s)
ρ	Fluid density (kg/m^3)
σ_k, σ_ε	Prandtl number for k and ε
υ	Kinematic viscosity (m^2/s)
$<T_{air}>$	Area-averaged air temperature (°C)
$<VR>$	Area-averaged wind velocity ratio
ΔT_{air}	Air temperature differences between the cool coating and no cool coating cases (°C)
ΔT_{sur}	Building surface temperature differences between the cool coating and no cool coating cases (°C)
2D, 3D	Two-dimensional, three-dimensional

1. Introduction

The world is undergoing rapid urbanization, with an increasing proportion of the global population residing in urban areas. The global urban population grew from 750 million to 4.22 billion during 1950–2018 and is projected to reach 6.68 billion by 2050 (United Nations, 2018). The boosting population, intensified land use, and rising anthropogenic heat emissions have contributed to a series of environmental challenges, particularly the worsening urban heat island (UHI) effect (Chen & Frauenfeld, 2016; Qiao et al., 2023; Xiang et al., 2024). The UHI phenomenon refers to the elevated ambient temperatures commonly observed in urban areas compared to adjacent rural surroundings. It has been demonstrated to significantly impact urban energy consumption, thermal comfort, urban air pollution, and public health (Cai et al., 2021; Li et al., 2019; Matthews et al., 2017). Therefore, it is of growing importance to implement effective urban cooling strategies for UHI mitigation.

Over the years, researchers have proposed a variety of urban cooling strategies, such as replacing regular construction surfaces with cool materials (Dimoudi et al., 2014; Santamouris et al., 2011), changing urban morphologies (Abd Elraouf et al., 2022; Chen et al., 2023), enhancing urban greening (Chang et al., 2024; Ren et al., 2024), and increasing urban water bodies (Hu et al., 2023; Sun & Chen, 2012). Among these, using cool materials is one of the most cost-effective approaches (Fabiani & Pisello, 2021). Cool materials have high solar reflectance and high infrared emissivity (Santamouris et al., 2011), which means less solar radiation absorption and more rapid heat release by long-wave radiation. Owing to this property, applying cool materials/cool coatings to urban roads (Chen & You, 2020; Georgakis et al., 2014) and building envelopes (Sinsel et al., 2021b; Taleghani et al., 2021; Xu et al., 2024a) can provide lower surface temperatures (Liu et al., 2024; Zeeshan & Ali, 2022), thereby improving the surrounding thermal environment (Donthu et al., 2024a; Elnabawi et al., 2023) and reducing building cooling energy consumption (Krayenhoff et al., 2021; Mandal et al., 2018; Zinzi, 2016).

Extensive studies, as summarized in **Table 1**, have substantiated the effectiveness of cool coatings in mitigating urban heat. These studies, encompassing microscale and mesoscale simulations as well as experiments across diverse climates (e.g., tropical, subtropical, temperate) and urban settings (e.g., idealized canyons, building arrays, and real urban regions), consistently report that cool coatings cause reductions in air temperature, significant surface cooling, and variable impacts on wind speed. In addition, some studies have also investigated the effect of cool coatings on the overall urban thermal environment. Previous studies (Li et al., 2014; Park & Baik, 2024; Reed & Sun, 2023) consistently report that the application of cool coatings increases the albedo of urban surfaces, thereby reducing the urban heat island (UHI) intensity. Li et al. (2014) observed that surface UHI and near-surface UHI get a 0.79 ℃ and 0.14 ℃ reduction with cool roofs when the albedo is increased by 0.2. Moreover, other studies (Donthu et al., 2024a; Elnabawi et al., 2023; Taleghani et al., 2021) have demonstrated that cool coatings can improve thermal comfort. Taleghani et al. (2021) conducted a microscale simulation study and revealed that cool walls contribute to improving the pedestrian thermal comfort (e.g., physiological equivalent temperature (PET) reduces by up to 1.0 ℃ with cool walls).

However, a common focus of these evaluations has been on meteorological factors (e.g., temperature and wind speed), while application cost is scarcely taken into consideration when assessing the performance of cool coatings. Such an omission of coating costs may mislead policymakers into implementing inappropriate or uneconomical cooling strategies. Hence, more effective and representative evaluation metrics are required to incorporate coating costs into the assessment of the cooling effect.

Moreover, in addition to the overlook of cost, the dependence of the cooling effect on specific building morphologies also deserves attention. Increasing evidence indicates that the performance of cool coatings varies with urban morphologies, such as street height-width-ratio (Li et al., 2024; Morini et al., 2018), plan area index (λ_p) (Hang et al., 2025; Liu et al., 2024; Lu et al., 2023; Sen & Khazanovich, 2021; Zhou et al., 2020), and sky view factor (Xu et al., 2024a). Specifically, Hang et al. (2025) found that cool coatings show more pronounced wall and indoor cooling effects in the low-density building array than in the medium-density one. Xu et al. (2023b) reported that cool materials show a greater cooling effect on slab-type buildings (length/width = 3) than point-type buildings (length/width = 1) at noon, while an opposite trend is observed in the morning and afternoon in Nanjing, China. Despite these advances, there remains an insufficient understanding of the synergy between cool coatings and various urban morphologies. In particular, the effects of street orientation and height variability on the performance of cool coatings are underexplored.

On one hand, previous parametric studies, either two-dimensional (2D) (Li et al., 2024; Park & Baik, 2024) or three-dimensional (3D) (Hang et al., 2025; Sinsel et al., 2021b; Taleghani et al., 2021), have relied on uniform-height (UH) building models, whereas real cities commonly feature varied-height (VH) buildings. Moreover, height variability can promote urban ventilation and improve pedestrian-level wind environments (Chen et al., 2017), benefiting urban heat removal (Adelia et al., 2019).

Therefore, it is worth investigating the synergistic effect of cool coatings and building height variability on urban cooling. On the other hand, street orientation significantly affects the amount of solar radiation received by east, west, south, and north walls of buildings, which may result in different cooling effects on each wall when cool coatings are applied (Taleghani et al., 2021). Accordingly, there is a need to unravel the performance of cool coatings under varying street orientations in 3D urban blocks.

To address the aforementioned research gaps, we conduct a parametric study to systematically examine the effects of cool coatings on roof and wall temperatures, as well as pedestrian-level microclimate, in 3D open high-rise building arrays with different street orientations (north-south and east-west) and building height layouts (UH and VH). Therefore, validated CFD simulations with turbulence model, radiation model, and solar load model are performed to simulate wind velocity and air-surface temperature fields under three summer solar heating conditions—8 am, 12 pm, and 4 pm. The meteorological background is set to Guangzhou, China—a highly urbanized, monsoon-influenced subtropical megacity facing severe UHI issues. Apart from cool roofs only (CR), we also consider their combinations with cool walls, including cool roofs and all walls (CR&W), cool roofs and east-west walls only (CR&EWW), and cool roofs and high-rise walls only (CR&HW). Cool roofs primarily lower the roof temperature and nearby air temperature, with limited cooling effects on the pedestrian-level microclimate and wall temperature (Hang et al., 2025; Lu et al., 2023). This limitation is particularly evident in open high-rise building arrays, which have large sun-exposed facade areas and inadequate shading from adjacent buildings. So, cool walls may be a good complement to cool roofs in enhancing wall cooling of high-rise buildings (Li et al., 2024; Zhu et al., 2021), which will be discussed in Section 3. Last but not least, we propose a novel indicator, named cooling intensity (*CI*, ℃/m^2), to measure the average surface temperature reduction contributed by each unit area of cool-coated surface to the entire building. Note that we use the area of cool-coated surfaces to represent coating costs.

The innovative contributions of this study include: (1) revealing the combined effects of street orientations and cool coatings on building surface temperatures and pedestrian-level microclimate in 3D high-rise building arrays; (2) quantifying the synergetic cooling effects of building height variability and cool coatings in 3D high-rise building arrays; (3) assessing the performance of CR&EWW and CR&HW in 3D high-rise buildings to achieve a balance between cooling effect and coating costs; (4) offering a more effective and feasible evaluation method by incorporating coating costs into the assessment of cooling effect. This study can facilitate the effective application of cool coatings in urban areas, thereby enhancing the efficiency of UHI mitigation strategies.

2. Methodology

2.1. Model descriptions, computational domain, and mesh generation

In line with the morphology characteristics of new urban areas in Guangzhou, the full-scale 3D ideal urban building array models are structured with open high-rise buildings (Rao et al., 2024). As shown in Fig. 1(a), the building array model consists of

63 slab buildings arranged in 9 rows and 7 columns. The basic building element has a dimension of 50 m × 12 m × 36 m in length (L), width (W), and height (H). The approaching wind is normal to longitudinal building walls. The x-, y-, and z-coordinate axes refer to the streamwise, spanwise, and vertical directions, respectively, with the coordinate origin located at the ground center of the building array. The widths of the streets in the streamwise and spanwise directions are 8 m (w_1) and 30 m (w_2), respectively. The central 3 × 3 building array (highlighted in blue) with adjacent half-streets is selected as the target study area (290 m × 210 m × 48 m) for subsequent analyses. To examine the effects of street orientation and building height variability, this study constructs three types of building array models for parametric comparisons, focusing on north-south versus east-west orientations and uniform building height versus alternating height variability. These two orientations are selected because they generally produce the most distinct contrasting interactions with solar angles and wind direction. Alternating height variability is designed as a simplified representation of urban heterogeneity. In all models, the approaching wind is kept perpendicular to the long-side building walls to isolate the effect of street orientation. As depicted in Fig. 1(b), the UH-NS model has uniform building height (UH), with long-side walls and wide streets extending north-south (N-S), and the approaching wind from the east. In the UH-EW model (Fig. 1(c)), the long-side walls and wide streets extend east-west (E-W), and the approaching wind comes from the south. In the varied-height model (VH-NS, in Fig. 1(d)), the even-row buildings are 48 m (H_2) tall, named high-rise buildings, while the odd-row ones maintain a height of H_1 = H = 36 m, named low-rise

buildings. Note that "high-rise" and "low-rise" are used here only in a relative sense. Therefore, comparing the UH-NS and UH-EW models can reveal the effect of street orientation, while comparing the UH-NS and VH-NS models can reveal the effect of height variability.

All buildings adopt identical cool coating configurations in a specific building array model, classified into five combinations (Fig. 1(e)): no cool coatings (NCC), cool roofs (CR), cool roofs & walls (CR&W), cool roofs & east-west walls (CR&EWW), and cool roofs & high-rise walls (CR&HW). The NCC case serves as the baseline for evaluating the effects of cool coatings. Comparison of CR&W and CR reveals the additional cooling contribution of cool walls across the three studied building arrays. CR&EWW and CR&HW represent optimized cool-coating strategies for uniform-height and varied-height models, respectively, in which cool coatings are omitted from surfaces receiving relatively low solar radiation. The optimization aims to balance the cooling effect and coating costs. In addition, to reveal the influence of different solar radiation heating and shading conditions, three representative local times—8 am, 12 pm, and 4 pm (LT08, LT12, and LT16) are examined. Consequently, a total of 36 cases are simulated, with detailed information listed in Table 2.

Following the best practice guidelines for CFD simulations (Franke et al., 2004; Tominaga et al., 2008), the computational domain is constructed with the inlet, lateral, upper, and outlet boundaries located at distances of $5H_{max}$, $5H_{max}$, $5H_{max}$, and $15H_{max}$ from the urban building array model, respectively. Here, H_{max} represents the maximum building height ($H_{max} = H_2 = 48$ m). Fluent Meshing is employed to generate meshes for all cases. Considering both computational cost and accuracy, polyhedral meshes are utilized to discretize the domain; mesh refinement with a growth rate of 1.05 is used for the target study area. Boundary layer meshes are set on all walls, including building surfaces and the ground, with the first layer mesh size set at 0.2 m. Before conducting the formal simulations, coarse, medium, and fine mesh arrangements are generated for the mesh sensitivity test for the UH-NS model without cool coatings at LT16, illustrated in Fig. 2. The total number of cells for the three mesh arrangements is 4.5 million, 5.3 million, and 7.9 million, respectively. Results of the mesh sensitivity test are discussed in Section 2.4.

2.2. Turbulence and radiation models

In CFD simulations, the steady Reynolds-Averaged Navier-Stokes (RANS) model is one of the most recognized turbulence modeling approaches (Alfonsi, 2009; Liu et al., 2025). It has gained widespread application in urban microclimate research (Blocken, 2015; Wang et al., 2025), owing to the satisfactory prediction accuracy, low computational costs, and accessible best practice guidelines (Blocken, 2018; Liu & Niu, 2016; Wang et al., 2025). Therefore, this study employs the steady RANS approach with the standard k-ε turbulence model and P-1 radiation.

The standard k-ε turbulence model has been proven to effectively simulate wind and thermal environments (Bottillo et al., 2014; Hang et al., 2013; Li et al., 2024; Liu et al., 2021), and thus, we select this model for our simulations. The steady-state governing equations for incompressible Newtonian fluids are as follows:

The mass conservation equation:

$$\frac{\partial \rho u_i}{\partial x_i} = 0 \tag{1}$$

The momentum conservation equation and thermal transport equation:

$$\frac{\partial \rho u_i u_j}{\partial x_j} = -\frac{\partial p}{\partial x_j} + \frac{\partial}{\partial x_j}\left(\mu_o \frac{\partial u_i}{\partial x_j}\right) - \beta g \rho \Delta T \delta_{ij} \tag{2}$$

$$\frac{\partial (\rho u_i T)}{\partial x_i} = \frac{\partial}{\partial x_i}\left(\Gamma_T \frac{\partial T}{\partial x_i}\right) + \frac{Q_T}{c_P} + \frac{1}{c_P}\left(\frac{\partial q_{ri}}{\partial x_i}\right) \tag{3}$$

The transport equations for the turbulent kinetic energy (k) and dissipation rate (ε):

$$\frac{\partial (\rho k u_i)}{\partial x_i} = \frac{\partial}{\partial x_j}\left[\left(\mu + \frac{\mu_t}{\sigma_k}\right)\frac{\partial k}{\partial x_j}\right] + P_k + P_b - \rho\varepsilon \tag{4}$$

$$\frac{\partial (\rho \varepsilon u_i)}{\partial x_i} = \frac{\partial}{\partial x_j}\left[\left(\mu + \frac{\mu_t}{\sigma_\varepsilon}\right)\frac{\partial \varepsilon}{\partial x_j}\right] + C_1 \frac{\varepsilon}{k}(P_k + P_b) - C_2 \frac{\rho \varepsilon^2}{k} \tag{5}$$

Where u_i and u_j are velocity components in the directions i and j (i, j = 1, 2, 3) of Cartesian coordinates. δ_{ij} is the Kronecker delta ($\delta_{ij} = 1$ when $i = j$; otherwise, $\delta_{ij} = 0$). ρ, p, μ, and $\mu_t = C_\mu \frac{\rho k^2}{\varepsilon}$ denote the air density, pressure, dynamic viscosity, and eddy viscosity, respectively. $\mu_o = \mu + \mu_t$ is the combination of dynamic viscosity (μ) and eddy viscosity (μ_t). The Boussinesq approximation is adopted to consider the thermal buoyancy effect. β, g, and T represent the thermal expansion coefficient, gravity acceleration, and air temperature, respectively. Γ_T, Q_T, and q_r indicate the effective thermal diffusivity, heat production rate, and radiative heat flux, respectively. c_p is the specific heat, equaling 1006.43 J·kg^{-1}·K^{-1} for air. $P_k = \mu_t \frac{\partial u_j}{\partial x_i}\left(\frac{\partial u_i}{\partial x_j} + \frac{\partial u_j}{\partial x_i}\right)$

and P_b are the turbulence production terms due to mean velocity gradients and buoyancy, respectively. $C_1 = 1.44$, $C_2 = 1.92$, and $C_\mu = 0.09$ are empirically model constants. $\sigma_k = 1.0$ and $\sigma_\varepsilon = 1.3$ are Prandtl numbers for k and ε.

This study adopts the P-1 radiation model to simulate radiative heat transfer, which has been widely applied in the CFD simulation of urban thermal environments (Antoniou et al., 2019; Buratti et al., 2018; Gromke et al., 2015; Hang et al., 2024; Liu et al., 2021; Toparlar et al., 2015). The P-1 radiation model takes into account the scattering effect and requires relatively low computational resources compared to other radiation models (Barbosa et al., 2023; Sazhin et al., 1996). Its capability to resolve radiative heat transfer has been validated by high-resolution thermal infrared satellite images (Toparlar et al., 2015) and meteorological data (Antoniou et al., 2019). Furthermore, the Solar Ray Tracing model is employed to simulate the radiation effects of incident solar rays. The sun direction vector and solar irradiation fluxes are computed from the built-in Solar Calculator based on geographical location, date, time, and mesh orientation (ANSYS Inc., 2023). This study inputs the longitude, latitude, and timezone of Guangzhou (23.13 °N, 113.29 °E, GMT+8) as the global position. The simulation date is specified as 15th July—the hottest day in Guangzhou during 2023 (NCEI, 2025). For the time of day, three typical times are considered, namely LT08, LT12, and LT16.

2.3. Boundary conditions and solver settings

As illustrated in Fig. 1(a), symmetry boundary conditions are applied to the lateral and upper boundaries of the domain. Velocity-inlet and pressure-outlet boundary conditions are imposed on the domain inlet and outlet, respectively. The inlet air temperatures for three local times (background temperatures) are set according to observations from the Guangzhou national benchmark meteorological station (NCEI, 2025) and are listed in Table 3. They represent the ambient inflow temperature at the domain inlet. The inlet profiles of wind velocity (U), k, and ε are defined as follows:

$$U(z) = \frac{U^{*}_{ABL}}{\kappa} \ln\left(\frac{z + z_0}{z_0}\right) \tag{6}$$

$$k(z) = \frac{{U^{*}_{ABL}}^{2}}{\sqrt{C_\mu}} \tag{7}$$

$$\varepsilon(z) = \frac{{U^{*}_{ABL}}^{3}}{\kappa(z + z_0)} \tag{8}$$

Where the roughness length (z_0) is set as 0.1 m, representing an open urban area with occasional large obstacles (WMO, 1996). κ = 0.41 is the von Karman constant. U^{*}_{ABL} is the friction velocity of the atmospheric boundary layer, calculated from the reference wind velocity (U_{ref} = 3 m/s) at the reference height of z_{ref} = 10 m:

$$U^{*}_{ABL} = \frac{\kappa U_{ref}}{\ln\left(\frac{z_{ref} + z_0}{z_0}\right)} \tag{9}$$

The reference Reynolds number ($Re = U_{ref}H/\upsilon,\ \upsilon = 1.46 \times 10^{-5} \mathrm{m}^2/\mathrm{s}$) is 7.4×10^6, satisfying the *Re*-independent similarity criterion (Zhu & Chew, 2023).

Table 4 presents the physical properties of materials used for wall boundaries. The material properties of uncoated building surfaces and ground are referenced from Toparlar et al. (2015). For cool-coated building surfaces, the material absorptivity and emissivity are set according to the commonly used authentic material properties, measured from our Scaled Outdoor Measurement of Urban Climate and Health

(SOMUCH) experiments (Hang et al., 2025). The non-slip shear condition is adopted for all wall boundaries. The non-dimensional distance $y+$ is ~400, justifying the application of the standard wall function for near-wall treatment (Blocken et al., 2007). Referring to Toparlar et al. (2015) and Chen et al. (2025), the Shell Conduction model is used for wall thermal boundary conditions. A shell model layer is set on the ground and building walls within the computational domain, with thicknesses of 10 m and 0.2 m and temperatures set at 10 °C and 25 °C, respectively. These values are justified as follows: soil temperature at about 10 m depth remains relatively stable all year round at roughly 10 °C (Popiel et al., 2001); the typical thickness of reinforced concrete exterior walls approximates to 0.2 m (Liu et al., 2020); summer indoor temperatures should be set at around 25 °C for thermal comfort (Li et al., 2025).

All CFD simulations are conducted using ANSYS Fluent 2023R1 (ANSYS Inc., 2023). The second-order upwind finite volume method is employed for the discretization of the governing equations. The Semi-Implicit Method for Pressure-Linked Equations (SIMPLE) algorithm is used to couple pressure and velocity. The relaxation factors are set to 0.3 for the pressure term, 0.7 for the momentum term, and 0.8 for both k and ε. The iterations continue until all residuals are smaller than 10^{-4} and converge.

2.4. Mesh sensitivity test

Fig. 3 compares normalized wind velocity (U/U_{ref}) and air temperature (T_{air}) distributions along three reference lines (Line V1, Line V2, Line H1) among coarse, medium, and fine mesh arrangements. Line V1 (x = 6 m, y = 0 m) and Line V2 (x = 0 m, y = 87 m) are vertical lines flushing against the building wall and located at the center of the streamwise street canyon, respectively; Line H1 (x = −21 m, z = 1.5 m) is located at the horizontal plane of z = 1.5 m. It is observed from the figure that the medium mesh provides very similar results to the fine mesh but has some distinctions with the coarse mesh in horizontal profiles.

Moreover, the grid convergence index (*GCI*) proposed by Roache (1997) is used to estimate the error in U/U_{ref} and T_{air} between mesh arrangements, as defined in Eqs. (10) and (11):

$$GCI = F_s \left| \frac{r^{pa}\left(U_m - U_{fine}\right)/U_{ref}}{1 - r^p} \right| \tag{10}$$

$$GCI_T = F_s \left| \frac{r^{pa}\left(T_{air,m} - T_{air,fine}\right)/T_{air,fine}}{1 - r^p} \right| \tag{11}$$

where F_s = 1.25 is the safety factor, $r = \sqrt{2}$ is the linear grid refinement factor, and pa = 2 is the formal order of accuracy corresponding to the used second-order discretisation schemes. U_m and $T_{air,m}$ denote the wind velocity and air temperature under the coarse or medium mesh arrangement, while U_{fine} and $T_{air,fine}$ represent the corresponding results on the fine mesh arrangement. As shown in Table 5, the average *GCI* values for the medium-fine comparison are below 2.1% for wind velocity and 0.2% for air temperature, and these values are smaller than those for the coarse-fine comparison. The *GCI* analysis confirms that the medium mesh arrangement provides grid-independent simulation results.

Consequently, this study opts to use the medium mesh arrangement for subsequent formal simulations.

2.5. CFD validation

2.5.1. Turbulent flow validation by wind tunnel experiments

Wind tunnel experiments by Lin et al. (2019) are used to verify the accuracy of the steady RANS method with the standard k-ε turbulence model in predicting steady flows within 3D building arrays of uniform height. As illustrated in Fig. A1, the wind tunnel model consists of regularly aligned cuboids, each 12 cm in height and 5 cm in both width and length. Velocity measurements are taken at Points V_i and M_i using the Laser Doppler Anemometer system. The validation study is performed on a full-scale model, scaled up by a factor of 600. Fig. A2 presents a comparison of experimental and simulated normalized stream-wise velocity ($\bar{u}/u_{ref}$) at the measurement points. The results indicate that the standard k-ε model outperforms the RNG k-ε model. The strong agreement between the experimental data and CFD simulation results confirms the reliability and accuracy of the standard k-ε model for turbulent flow simulation within uniform-height 3D building arrays.

Subsequently, wind tunnel experiments by Chen et al. (2017) are utilized to validate the accuracy of the standard k-ε model for 3D building arrays with varied heights. Fig. A3 shows the geometry and dimensions of the experimental model, which comprises 25 rows and 15 columns of cuboids, with alternating low-rise and high-rise rows. Similarly, the validation uses a full-scale model scaled up by 500 relative to the experimental model. Fig. A4 compares the normalized velocity profiles obtained from experiments and CFD simulations. The good agreement between experimental and simulated results demonstrates the accuracy of the standard k-ε model in simulating turbulent flows within 3D building arrays featuring height variability.

Overall, these validation studies demonstrate that the steady RANS method with the standard k-ε model is reliable for simulating turbulent flows in 3D building arrays with both uniform and varied building heights. Detailed wind tunnel experimental setups and validation studies can refer to our previous works (Chen et al., 2017; Lin et al., 2019; Sha et al., 2018; Zhang et al., 2020).

2.5.2. Heat transfer and radiation validation by scaled outdoor experiments

Rigorous validation of radiative heat transfer simulations is often challenging, primarily due to data uncertainty and complex boundary conditions (Huo et al., 2021). Our SOMUCH platform addresses these issues by enabling high-quality and high-resolution parametric measurements of wind speed and air-surface temperature under realistic meteorological conditions (Chen et al., 2020). Therefore, scaled outdoor experiments by Chen et al. (2025) are used to validate CFD simulations coupling the standard k-ε model turbulence model with the P-1 radiation model and solar load model. The scaled experimental setup and its computational domain are shown in Fig. B1. Each concrete cuboid measures 1.2 m high, 0.5 m wide and long, with a wall thickness of 0.015 m.

Fig. B2 compares experimental and simulated surface temperatures, wind speeds, and air temperatures for different turbulence (standard k-ε, RNG k-ε, Realizable k-ε, and SST k-ω) and radiation models (P-1, Discrete Ordinates (DO), and Surface-to-Surface (S2S)). Table B1 presents the corresponding statistical metrics, including the mean absolute error (MAE), root mean square error (RMSE), and coefficient of determination (R^2). The results show that the standard k-ε model achieves satisfactory agreement with experimental data, and the RNG k-ε, Realizable k-ε, and SST k-ω models do not show apparent improvements. For radiation models, although DO and S2S models provide better predictions of surface temperature, the P-1 model still produces acceptable results, with discrepancies relative to experimental data only slightly greater than those of DO and S2S. Moreover, all three radiation models show highly consistent accuracy in simulating air temperature and wind speed. Hence, we still select the P-1 model for all radiation simulations, considering its computational efficiency and acceptable accuracy. This selection is also supported by the successful application of the P-1 model in realistic urban thermal environment simulations by Toparlar et al. (2015) and Antoniou et al. (2019). A detailed account of this validation study can be found in our previous study (Chen et al., 2025).

Considering the above reliable evidence, this study can safely apply the standard k-ε turbulence model with the P-1 radiation model and solar load model to simulate the turbulence, radiation, and heat transfer in 3D full-scale urban building arrays.

2.6. Cool coating performance evaluation

As mentioned previously, this study only focuses on the target building area (see Fig. 1) located in the middle of the entire model to exclude potential errors from surrounding buildings. Five indices, namely $<VR>$, $<T_{air}>$, ΔT_{sur}, CM, and CI, are proposed to evaluate the impacts of cool coating on pedestrian-level wind velocity (U) and air temperature (T_{air}) as well as building surface temperature (T_{sur}). The area-averaged wind velocity ratio ($<VR>$) and air temperature ($<T_{air}>$) within the target study area at the pedestrian level (z = 2 m) are calculated to indicate pedestrian-level wind and thermal environments. Here, *VR* is the mean wind velocity normalized by the reference wind velocity (U_{ref}). ΔT_{sur} is the surface temperature difference between the cool coating and no cool coating cases, measuring the temperature drop induced by cool coating.

$$\Delta T_{sur} = T_{sur,CC} - T_{sur,NCC} \tag{12}$$

Where the subscripts of CC and NCC represent cool coating and no cool coating cases, respectively.

In practical applications, the integrated temperature drop of building envelopes has a crucial effect on building cooling energy consumption. Cooling magnitude is defined as the ensemble average of $\overline{\Delta T_{sur}}$ across all target buildings over all local times, for each specific combination of cool coating configuration and urban morphology. Here, ΔT_{sur} is the area-weighted average surface temperature drop per building. Krayenhoff et al. (2021) defined cool effectiveness as the ratio of the air temperature difference to the principal change associated with the heat mitigation implementation. Based on this definition, we further specify the ratio of $\overline{\Delta T_{sur}}$ to the cool-coated surface area as cooling intensity (*CI*) with a unit of °C/m^2. This new index represents the average surface temperature drop contributed by each unit of cool-coated surface area to the entire building.

Ultimately, the overall cooling performance of cooling coatings on building surfaces can be quantified by two cooling indices of *CM* and *CI*.

$$\overline{\Delta T_{sur}} = \frac{\int \Delta T_{sur} dA}{\int dA} \tag{13}$$

$$CM = \frac{\sum_{t=1}^{TM} \sum_{b=1}^{B} \overline{\Delta T_{sur}}_{(t,b)}}{TM \times B} \tag{14}$$

$$CI = \frac{\overline{\Delta T_{sur}}}{A_{CC}} \tag{15}$$

Where A represents the area of the mesh cell, and A_{cc} is the ensemble area of cool-coated surfaces per building. TM = 3 is the simulated local times in a given urban morphology and coating configuration, and B = 9 is the number of target buildings per case. t and b are the corresponding counters.

3. Results and discussion

3.1. Impacts of street orientations and cool coatings

3.1.1. Building surface temperature (T_{sur})

To reveal the combined effects of street orientations and cool coatings, this subsection first analyzes the common spatial characteristics of T_{sur} in uniform-height building arrays without cool coatings, then clarifies the difference between UH-NS and UH-EW models, and finally unravels the cooling effect of cool coatings on T_{sur} by comparing NCC and CR&W cases.

Fig. 4(a–b) shows the contour plots of T_{sur} in UH-EW and UH-NS models without cool coatings at different local times. At LT08, the highest-temperature region (T_{sur} = ~39 °C) is observed on the east walls, despite being partially shaded (T_{sur} = ~31 °C) by adjacent buildings. This result occurs because the sun is located in the east-northeast with a low solar altitude (Table 3). Consequently, partial east and north walls, as well as roofs, are exposed to direct sunlight, while west and south walls face away from the sun. Meanwhile, among these sunlit areas, east walls receive the most intense solar radiation and thus are classified as direct sunlit zones, whereas roofs (T_{sur} = ~35 °C) and north walls (T_{sur} = ~33 °C) receive direct sunlight at a low angle, forming oblique sunlit zones. At LT12, with the solar altitude being nearly vertical (Table 3), the roofs receive the most intense solar radiation, resulting in a peak T_{sur} of ~51 °C. In contrast, vertical facades are nearly parallel to the direction of sunlight, thus receiving little direct sunlight and experiencing negligible mutual shading. The maximum temperature difference exceeds 10 °C between the roofs and walls at this time. At LT16, as the sun is slightly north of due west (Table 3), direct sunlit zones of the west walls receive the most intense solar radiation, forming the highest-temperature region (T_{sur} = ~46 °C) among all building surfaces. Compared to LT08, the current solar altitude increases significantly (Table 3). Consequently, at LT16, the overall surface temperature rises; direct sunlit zones expand while mutually shaded zones shrink; and roofs receive more solar radiation, narrowing their temperature gaps relative to the direct sunlit zones.

Despite these shared spatiotemporal distributions of surface temperature, UH-NS and UH-EW models demonstrate pronounced differences in the size and temperature of direct sunlit zones. As depicted in Fig. 4(a–b), east-west walls are the smallest facades in the UH-EW model, whereas they become the largest facades in the UH-NS model. Therefore, the UH-EW model exhibits significantly smaller direct sunlit zones on east walls in the morning and on west walls in the afternoon, compared to the UH-NS model. Moreover, in the UH-EW model, the proportion of direct sunlit zones relative to the entire east-west walls is minimal due to the narrow street canyons, and the temperature of direct sunlit zones is ~1 °C lower than in the UH-NS model.

The cooling effect of cool coatings on T_{sur} is analyzed below. Fig. 4(c) presents the spatial distribution of T_{sur} in the UH-NS model under CR&W. Although all roofs and walls are cool-coated, direct sunlit zones consistently exhibit the highest surface temperature at each time. For example, temperature differences between direct sunlit and shaded zones reach ~2 °C at LT08 and LT16. Compared to NCC (Fig. 4(b)), CR&W significantly reduces T_{sur} on direct sunlit zones of east-west walls at LT08 and LT16, with moderate cooling effects on roofs, while leaving shaded zones nearly unaffected; at LT12, CR&W exerts the greatest temperature drop on direct sunlit roofs, with slight cooling effects on vertical facades. This phenomenon is attributed to the critical property of cool coatings that decreases heat adsorption through high solar reflectance. Consequently, cool coatings exhibit better cooling performance on surfaces receiving more direct sunlight.

The contour plots of surface temperature drop (ΔT_{sur}) offer more intuitive evidence of the cooling effect induced by CR&W, which are illustrated in Fig. 5(a). By definition, the smaller the ΔT_{sur}, the greater the surface temperature drop (i.e., the stronger the cooling effect). ΔT_{sur} shows evident spatio-temporal variation patterns. At LT08 and LT16, direct sunlit zones on the east-west walls undergo the highest temperature drop (4.0–7.0 °C) among all building surfaces, followed by the oblique sunlit roofs (2.5–5.0 °C), and the least shaded zones (~0 °C). Meanwhile, roofs experience a greater temperature drop at LT16 (~4.2 °C) than at LT08 (~2.6 °C). At LT12, direct sunlit roofs demonstrate the greatest temperature drop (6.0−7.5 ℃), markedly higher than that on vertical facades (< 2.0 ℃). Moreover, comparing UH-EW (Fig. 5(b)) and UH-NS models (Fig. 5(a)) reveals that street orientation hardly modifies ΔT_{sur} on roofs, but significantly affects values on walls. Owing to its larger direct sunlit zones, the UH-NS model shows wider coverage of strong cooling on east-west walls than the UH-EW model at LT08 and LT16. Here, we consider $\Delta T_{sur} \leq -4.0$ ℃ as strong cooling. Comparable results are observed under CR and CR&EWW, as evidenced in Figs. C1 and C2. CR&EWW demonstrates nearly identical temperature drop patterns with CR&W, while CR affects almost exclusively roof temperatures with little influence on wall temperatures. In brief, cool coatings mainly act on cool-coated surfaces, significantly reducing surface temperatures in direct sunlit zones with minimal cooling effects in shaded zones. Li et al. (2024) reported a similar finding in 2D street canyons with various cool coatings.

Overall, for uniform-height building arrays, the highest-temperature region is observed on the roofs at noon, on east walls in the morning, and on west walls in the afternoon. Street orientation and canyon width significantly affect the size and temperature of direct sunlit zones in the morning and afternoon, thus impacting surface temperature distributions. Cool coatings primarily reduce the temperature of direct sunlit zones and hardly cool shaded zones.

3.1.2. Area-averaged wind velocity ratio (<*VR*>) and air temperature (<T_{air}>)

This subsection examines the combined effects of street orientations and cool coatings on pedestrian-level microclimate based on the area-averaged wind velocity ratio and air temperature. Fig. 6 shows variations of pedestrian-level $<VR>$ and $<T_{air}>$ with street orientations and cool coating configurations at three local times. Both wind velocity and air temperature exhibit significant temporal variations. As exemplified by NCC cases, $<VR>$ reaches its peak (~0.3) at LT12, 0.08–0.16 higher than its values at LT08 and LT16 (Fig. 6(a–b)). This result is attributed to stronger buoyancy-driven convection at noon compared to LT08 and LT16, as indicated by inter-surface temperature differences in Fig. 4(a–b). In contrast, $<VR>$ exhibits minor variation ($<$ 0.06) between UH-NS and UH-EW models. Regarding pedestrian-level air temperature (Fig. 6(c–d)), all cases experience notably higher $<T_{air}>$ at LT12 and LT16 compared to LT08. Taking NCC cases as examples, the difference in $<T_{air}>$ exceeds 10 °C between LT12 and LT08, but is within 1.1 °C between LT12 and LT16. This result agrees with a typical daytime temperature variation trend during summer. By contrast, the $<T_{air}>$ difference between UH-NS and UH-EW models is minor (no more than 0.5 °C), and in most cases, the UH-NS model exhibits slightly lower air temperatures. The above results demonstrate that street orientation (N-S vs. E-W) exerts limited influence on pedestrian-level wind velocity ($<$ 0.06) and air temperature ($<$ 0.5 °C) in uniform-height building arrays, regardless of cool coating configurations.

Similar to street orientation, cool coating has minor effects on pedestrian-level wind velocity ($<$ 0.06), especially in the UH-EW model ($<$ 0.01). Moreover, in contrast to NCC cases, all cool coating cases demonstrate a minor reduction ($<$ 0.3 °C) in pedestrian-level air temperature, irrespective of street orientations. Despite a minor cooling effect, CR&W still exhibits a relatively stronger cooling effect on pedestrian-level air temperature (0.08–0.24 °C) compared to CR (0–0.18 °C) and CR&EWW (0.03−0.23 °C). Our results are in line with previous studies (Donthu et al., 2024a; Li et al., 2024; Wang et al., 2023) on the effects of cool building envelopes on in-canyon airflow and air temperature. For example, Xu et al. (2024c) reported that application of cool materials on building surfaces has little effect on wind speed; Lu et al. (2023) observed that CR and CR&W only induce a maximum reduction of 0.4 °C in street T_{air} in Guangzhou during summer by scaled outdoor experiments; Sinsel et al. (2021a) revealed that super cool roofs decrease the pedestrian-level T_{air} in New York City by up to 0.49 °C by ENVI-met.

In conclusion, both pedestrian-level wind velocity and air temperature vary significantly with changes in solar radiation heating in uniform-height building arrays. In contrast, modifying street orientation and cool coating configuration exhibits only a slight cooling effect on air temperature and minimal impact on wind velocity.

3.2. Impacts of building height variability and cooling coatings

3.2.1. Building surface temperature (T_{sur})

To reveal the combined effects of building height variability and cool coatings, this subsection first compares the spatial distributions of T_{sur} between UH-NS and VH-NS models under NCC and CR&W. Then, the focus turns to the temperature drop induced by CR&W in the VH-NS model versus the UH-NS model.

Fig. 7(a–b) demonstrates the distribution of T_{sur} in the VH-NS model under NCC and CR&W at different local times. Similar to the UH-NS model (Fig. 4(b–c)), the highest-temperature region in the VH-NS model occurs on direct sunlit zones of the east walls at LT08, the roofs at LT12, and the west walls at LT16, irrespective of cool coating configurations. Meanwhile, the VH-NS model exhibits comparable surface temperatures to the UH-NS model in direct sunlit, oblique sunlit, and shaded zones. However, in the VH-NS model, height variability causes different sizes of direct sunlit and shaded zones on east-west walls between high-rise and low-rise buildings at LT08 and LT16. Specifically, compared to the UH-NS building array, high-rise buildings have larger direct sunlit zones and nearly identical shaded zones due to their extended east-west wall areas and less shading from adjacent buildings; conversely, low-rise buildings exhibit smaller direct sunlit zones and larger shaded zones because of more shading from adjacent buildings. At LT12, the high solar altitude minimizes mutual shading between buildings. Therefore, despite a distinct height layout between them, UH-NS and VH-NS models share similar surface temperature distributions. In brief, height variability mainly influences the size of direct sunlit and shaded zones on east walls in the morning and west walls in the afternoon, resulting in expanded direct sunlit zones in high-rise buildings but narrowed direct sunlit zones with expanded shaded zones in low-rise buildings.

Fig. 7(c) shows the contour plots of surface temperature drop (ΔT_{sur}) in the VH-NS model at different local times, indicating the cooling effect of CR&W on surface temperatures. Analogous to the UH-NS model (Fig. 5(a)), the VH-NS model displays the highest temperature drop on direct sunlit zones of east-west walls at LT08 and LT16 and on roofs at LT12, with negligible cooling effects on shaded zones at each time. The most significant difference between VH-NS and UH-NS models lies in the size of strong cooling zones ($\Delta T_{sur} \leq -4.0$ °C) in the morning and afternoon. Height variability results in a smaller coverage of strong cooling on east-west walls in low-rise buildings at LT08 and LT16, but a larger coverage in high-rise buildings. Notably, although this study limits height variability between high-rise and low-rise buildings to 12 m, height heterogeneity between high skyscrapers and low buildings is generally higher in reality. Consequently, when the solar altitude is low, shadows caused by high-rise buildings may cover entire low-rise buildings, considerably moderating the cooling effect of cool coatings on low-rise buildings. This is the motivation for studying the CR&HW configuration in varied-height building arrays. Contour plots of ΔT_{sur} under CR and CR&HW are presented in Fig. C3. Both configurations primarily exert cooling effects on cool-coated surfaces. Meanwhile, Fig. 7(c) and Fig. C3 suggest that CR and CR&W show visually comparable cooling effects on roofs, while CR&HW and CR&W demonstrate visually similar cooling effects on high-rise buildings and low-rise roofs. Subsection 3.3 will provide a detailed comparison of cooling performance between CR, CR&W, and CR&HW using quantitative metrics.

To sum up, under the identical street orientation, varied-height building arrays demonstrate analogous spatio-temporal distributions of T_{sur} and ΔT_{sur} in direct sunlit, oblique sunlit, and shaded zones to uniform-height building arrays. Nevertheless, height variability significantly changes the size of direct sunlit and shaded zones in high-rise and low-rise buildings at low solar altitudes, thus modifying the area of strong cooling coverage in these two buildings with cool coatings.

3.2.2. Area-averaged wind velocity ratio (<*VR*>) and air temperature (<T_{air}>)

Fig. 8 illustrates the area-averaged wind velocity ratio (<*VR*>) and air temperature (<T_{air}>) at pedestrian level (z = 2 m) in the VH-NS model with various cool coatings at different local times. Both wind velocity and air temperature exhibit significant temporal variations in the VH-NS model, while changing little with coating configurations. Taking NCC cases as an example, the stronger buoyancy-driven convection results in <*VR*> peaking at 0.29 at LT12, 0.08–0.14 higher than its values at LT08 and LT16 (Fig. 8(a)). In contrast, the difference in <*VR*> among coating configurations is minimal. CR shows nearly identical <*VR*> to NCC, while CR&W and CR&HW are 0.01–0.03 lower. Concerning pedestrian-level air temperature (Fig. 8(b)), all cases reach the highest <T_{air}> of ~41.5 °C at LT12, notably higher than 30.8−30.9 °C at LT08 and slightly greater than 40.4–40.7 °C at LT16. Compared to NCC cases, all cool coating cases demonstrate minor reductions of 0.01–0.27 °C in pedestrian-level air temperature across three local times; both CR&W (0.09–0.21 °C) and CR&HW (0.09–0.27 °C) exhibit more significant cooling effects on air temperature compared to CR (0.01–0.04 °C). Both cool roofs and cool walls reduce pedestrian-level air temperatures. However, the cooling effect of cool walls is significantly greater than that of cool roofs. Although applying cool coatings on roofs can effectively reduce roof surface temperatures, pedestrian-level air temperature is primarily influenced by the surrounding walls and ground. Consequently, the cooling effect of cool roofs at the pedestrian level is relatively small. In contrast, applying cool coatings on walls reduces wall surface temperatures, thereby decreasing air temperature through convection heat transfer within the street canyon. Nevertheless, cool walls can also increase reflected solar radiation within the street canyon, potentially raising the air temperature. Notably, CR&HW has a slight advantage over CR&W in reducing air temperature. This phenomenon may be attributable to the fact that leaving low-rise walls uncoated in CR&HW reduces multiple reflections within the street canyon. The use of high-albedo cool coatings on walls enhances multiple reflections, potentially causing slight warming of air and uncoated or shaded walls (Li et al., 2024). This air warming effect moderates air temperature drops induced by low surface temperatures. Consequently, benefitting from fewer multiple reflections, CR&HW results in a greater air temperature drop compared to CR&W.

Similar to cool coating configuration, building height variability exerts a marginal influence on pedestrian-level wind velocity, as evidenced by comparing Fig. 8(a) with Fig. 6(b). The difference in $<VR>$ between UH-NS and VH-NS models is below 0.02 across NCC, CR, and CR&W at three local times. Moreover, the VH-NS model displays a lower $<T_{air}>$ than the UH-NS model (Fig. 6(d)) under identical coating configurations and solar heating conditions, although the decrement is within 0.4 °C. The above results indicate that height variability (UH vs. VH) hardly affects pedestrian-level wind velocity but slightly decreases air temperature.

In conclusion, solar radiation heating plays a greater role in pedestrian-level microclimate than cool coating configuration and building height variability in varied-height building arrays. Both height variability and cool coatings slightly reduce air temperature but negligibly affect wind velocity; applying cool coatings on roofs and walls is more effective than coating roofs alone in changing wind velocity and air temperature.

3.3. Quantitative evaluation of the cooling performance of cool coatings

3.3.1. Comparison of ΔT_{sur} among different building surfaces

According to the preceding analysis, cool coatings exhibit a significant cooling effect on building surfaces. Based on descriptive statistical analysis, this subsection further quantifies the combined effects of coating configuration, street orientation, and height variability on the cooling performance of cool coatings on north-south walls, east-west walls, and roofs.

Fig. 9 statistically presents the distribution of ΔT_{sur} on north-south walls, east-west walls, and roofs across different urban morphologies under various cool coating configurations. The box shows the quartiles of the dataset, with the whiskers indicating the rest of the distribution; hollow geometries denote the mean, while the horizontal line represents the median. On average, CR&W (Fig. 9(a)) results in the greatest temperature drop on roofs (4.40–4.92 °C), followed by east-west walls (0.51–1.51 °C), and then north-south walls (0.19–0.32 °C). The reason is that roofs receive the most direct sunlight during the daytime, while north-south walls receive the least. Considering the effects of street orientation, UH-NS and UH-EW models experience almost identical temperature drops on roofs, averaging ~4.4 °C. However, on average, for east-west walls, the UH-NS model exhibits a 0.83 °C greater temperature drop than the UH-EW model, while for north-south walls, the UH-EW model displays a 0.08 °C greater temperature drop than the UH-NS model. Therefore, changing street orientation from E-W to N-S primarily enhances cool coatings' cooling effect on east-west walls, with little variation on roofs and north-south walls. This finding is also applicable under CR and CR&EWW (Fig.9(b-c)). In addition, contrasting UH-NS and VH-NS models reveals that height variability enhances the cooling effect on low-rise building roofs and high-rise building walls but weakens the cooling effect on low-rise building walls and high-rise building roofs. This result is primarily due to the following causes. First, height variability severely lowers wind velocity near the roofs of low-rise buildings, impairing convective heat transfer (Chen et al., 2017). Thus, low-rise roof temperatures are more responsive to reduced solar heat absorption, exhibiting greater drops under cool coatings (Li, 2025). High-rise roof temperatures exhibit the opposite mechanism, showing slightly smaller drops due to amplified wind velocity. Second, low-rise building roofs receive additional long-wave radiation from adjacent high-rise building walls, thereby gaining an extra cooling effect from cool high-rise building walls. The cooling discrepancy on walls is previously explained in subsection 3.2.1.

Moreover, Fig. 9(b–d) quantitatively demonstrates that CR, CR&EWW, and CR&HW hardly cool uncoated building surfaces. For coated walls and roofs, CR&EWW shows an intermediate cooling effect between CR&W and CR in both UH-NS and UH-EW models, indicating a cooling enhancement by supplementing cool walls. In contrast, in the VH-NS model, CR&HW exhibits a marginally stronger cooling effect than CR&W. This phenomenon may stem from fewer multiple reflections between coated-uncoated surfaces compared to coated-coated surfaces. High-rise building walls receive less reflected solar radiation from opposite low-rise building walls under CR&HW, thereby exhibiting greater temperature drops. The resulting lower wall temperatures of high-rise buildings further reduce the roof temperatures of low-rise and high-rise buildings by radiative and conductive heat transfer, respectively.

To summarize, cool coatings show the strongest average cooling effect on roofs, followed by east-west walls, and finally north-south walls. Among coating configurations, CR demonstrates the worst cooling performance as its cooling effect is mostly limited to roofs. Street orientation primarily affects the temperature drop of east-west walls, with marginal effects on other building surfaces. Height variability influences high-rise and low-rise buildings differently, as indicated by enhanced effects of cool coatings on low-rise roofs and high-rise walls.

3.3.2. Cooling magnitude (*CM*)

Following a segmented analysis of north-south walls, east-west walls, and roofs, this subsection moves focus to a holistic evaluation of entire building envelopes, quantifying the ensemble-average surface temperature drop, namely cooling magnitude, for each specific urban morphology and cool coating configuration combination.

Fig. 10(a) compares *CM* values in nine combinations of urban morphology and cool coating configuration. By definition, the smaller the *CM* value, the greater the cooling magnitude. Overall, cool coatings can reduce T_{sur} by 0.36–1.63 °C, with the magnitude differing in coating configuration, street orientation, and building height layout. For uniform-height building arrays, the UH-NS model achieves a greater cooling magnitude compared to the UH-EW model, regardless of cool coating configurations; the *CM* difference between these two street orientations reaches 0.89 °C under CR&EWW, followed by 0.69 °C under CR&W and 0.03 °C under CR. Moreover, comparing the three cool coating configurations reveals that CR provides the lowest cooling magnitudes (0.47–0.50 °C), while CR&W causes the highest ones (0.83–1.52 °C). Meanwhile, *CM* variation with cool coating configuration is more significant in the UH-NS model than in the UH-EW model. Specifically, in contrast to only cool roofs, the supplement of cool walls can further cool the overall building surface by 1.02 °C (CR&W minus CR) in the UH-NS model, primarily contributed by cool coatings on east-west walls (0.97 °C by CR&EWW minus CR). Besides, although cool north-south walls contribute little to *CM* value (0.05 °C) in the UH-NS model, they cause an additional building surface cooling of 0.25 °C (CR&W minus CR&EWW) in the UH-EW model.

The cooling magnitude of the VH-NS model varies with cool coating configuration and building height. First, compared to low-rise buildings, high-rise buildings experience a 0.18 °C lower cooling magnitude under CR, but a 0.38 °C and 0.97 °C greater cooling magnitude under CR&W and CR&HW, respectively. Second, a comparison of VH-NS and UH-NS models reveals that height variability shows contrasting effects on high-rise and low-rise buildings. For high-rise buildings, height variability decreases cooling magnitude by 0.14 °C under CR but causes a marginal increase under CR&W. Conversely, for low-rise buildings, it slightly enhances cooling magnitude under CR but reduces it by 0.35 °C under CR&W. Third, CR&W results in greater cooling magnitudes than CR for both high-rise and low-rise buildings, corresponding with results in the UH-NS model. Fourth, based on cool roofs, adding cool coatings on high-rise building walls significantly enhances the cooling magnitude of high-rise buildings by 1.19 °C (CR&W minus CR). In contrast, the same addition to low-rise building walls offers only a 0.63 °C increase in low-rise buildings. The reason for the nearly halved increment is that most low-rise building walls are shaded by high-rise buildings at LT08 and LT16, thereby reducing the effective cool-coated surface area of low-rise buildings. Last, CR&HW enhances the cooling magnitude of high-rise buildings by 0.08 °C relative to CR&W. Although low-rise buildings do not have cool-coated walls under CR&HW, their cooling magnitude still increases by 0.12 °C relative to CR. This result is consistent with Fig. 9, with possible causes previously analyzed in subsection 3.3.1.

In summary, the cooling magnitude of the UH-NS model is more sensitive to changes in cool coating configuration than that of the UH-EW model. Adding cool coatings on east-west walls enhances cooling magnitude more effectively in the UH-NS model than in the UH-EW model. Height variability slightly enhances cooling magnitude in high-rise buildings but sharply reduces it in low-rise buildings under CR&W; however, the effect of height variability is reversed under CR. Furthermore, without adding extra coatings, CR&HW provides higher cooling magnitudes than CR&W in high-rise buildings and than CR in low-rise buildings.

3.3.3. Cooling intensity (*CI*)

In addition to cooling magnitude, the cost of using cool coatings should also be taken into account in the holistic evaluation. Therefore, the following subsection focuses on contrasting cooling intensity, the average surface temperature drop per unit of cool-coated surface area, among various combinations of urban morphology and cool coating configuration.

Fig. 10(b) illustrates variations of *CI* value with street orientation, building height layout, and cool coating configuration. The box shows the quartiles of the dataset, with the whiskers indicating the maximum and minimum values; hollow circles denote the mean, while the horizontal line represents the median; solid circles stand for *CI* per building. Owing to *CI* being negative, the smaller the value, the greater the cooling intensity. For uniform-height building arrays, CR achieves the highest cooling intensity, averaging 7.91×10^{-4} °C/m^2 in the UH-EW model and 8.26×10^{-4} °C/m^2 in the UH-NS model, respectively. Although CR&W can provide the greatest ensemble-average temperature drop (Fig. 10(a)), this configuration yields the lowest cooling intensity due to the large cool-coated area. Compared to CR&W, removing cool coatings on north-south walls (i.e., CR&EWW) can increase cooling intensity by ~142.3% in the UH-EW model and ~17.4% in the UH-NS model. Besides, in comparison with the UH-EW model, the UH-NS model has a greater cooling intensity under CR and CR&W, but a lower one under CR&EWW. This result, alongside consistently greater cooling magnitude, demonstrates that cool coatings generally achieve superior cooling performance in N-S oriented building arrays compared to E-W oriented arrays.

For varied-height building arrays (the VH-NS model), both high-rise and low-rise buildings show greater cooling intensity under CR than under CR&W. Low-rise buildings experience superior cooling magnitude and intensity compared to high-rise buildings under CR. In contrast, under CR&W, despite a distinct cooling magnitude, the two types of buildings have almost identical cool intensities. This is because no extra cooling intensity is generated by the additional cool-coated area of high-rise buildings over low-rise buildings. Furthermore, contrasting CR&HW with CR&W demonstrates that omitting cool coatings on low-rise walls increases the cooling intensity of high-rise buildings by ~5.1%. A comparison between CR&HW and CR shows that adding cool coatings on high-rise walls contributes to low-rise buildings achieving maximum cool intensity, with an average of 10.96×10^{-4} °C/m^2. In addition, relative to the UH-NS model, high-rise buildings exhibit a ~27.6% decrease in cooling intensity under CR, whereas low-rise buildings show a ~9.9% increase; all buildings witness a cooling intensity decrease under CR&W. Hence, considering both cooling intensity and magnitude, height variability enhances the cooling performance of low-rise buildings under CR but reduces it under CR&W; however, the cooling performance for high-rise buildings declines under both configurations.

Fig. 10(b) also indicates that cooling intensity by CR shows the most pronounced temporal variation, followed by CR&EWW and CR&HW, and then CR&W, irrespective of street orientation and building height layout. Furthermore, CR always provides the greatest cooling intensity at LT12 and the lowest value at LT08 for all types of building arrays. However, CR&EWW and CR&W show distinct cooling intensities from CR in the UH-NS model, with the maximum occurring at LT16 and the minimum existing at LT12. This indicates that in the UH-NS model, adding cool coatings to walls can significantly enhance cooling intensity with low-angle direct sunlight (i.e., LT08 and LT16). The only difference between UH-NS and VH-NS models is that CR&W and CR&HW generate the lowest cooling intensity at LT08 for low-rise buildings, owing to the large area shaded on low-rise buildings.

In conclusion, for uniform-height building arrays, CR consistently offers the highest cooling intensity, while CR&W yields the lowest cooling intensity due to increased cool-coated surface area. For varied-height building arrays, CR&HW enhances cooling intensity over CR in low-rise buildings and over CR&W in high-rise buildings.

3.4. Discussion and design implications

This study indicates that cool coatings significantly reduce building surface temperatures (by up to 7.5 °C), with this cooling performance varying with street orientation, building height layout, and cool coating configuration. In contrast, the effect of cool coating on perdestrain-level air temperature and wind velocity is minor, with air temperature drops below 0.3 °C and normalized wind velocity variations less than 0.6.

Contextualized within existing literature, our results are comparable with several previous findings that cool coatings reduce building surface temperature by up to 4−15 °C (Hang et al., 2025; He et al., 2020; Xu et al., 2024b) and pedestrian-level air temperature by less than 1 °C (Lu et al., 2023; Zeeshan & Ali, 2022; Zhu et al., 2021). However, the magnitude of air temperature reduction we observe is substantially smaller than some earlier studies. Several works report that the air temperature drop at the pedestrian level exceeds 1 °C (Donthu et al., 2024a; Wang et al., 2023; Zhou et al., 2020). This discrepancy can be attributed to two reasons. First, we analyze an area-averaged air temperature for the pedestrian level. This approach can smooth out stronger local cooling (i.e., larger air temperature drop). Second, our simulations employ the CFD method, with the model only covering 400 m × 400 m. Previous studies that observed larger air temperature drops mostly employed mesoscale simulations (Liu & Morawska, 2020; Wang et al., 2023; Zhou et al., 2020). Within microscale simulations, our results are indeed consistent with other studies (Elnabawi et al., 2023; Li et al., 2024; Sinsel et al., 2021b). This discrepancy between microscale and mesoscale models is supported by Sinsel et al. (2021a), who reported significant model differences in the maximum air temperature cooling between nested microscale and mesoscale simulations when examining the cooling effect of super cool roofs on two cities.

Furthermore, this study introduces two indices (cool magnitude and cool intensity) to evaluate the performance of cool coatings. Based on these indices, we derive some design implications for applying cool coatings to urban cooling from both cooling effect and cost-effectiveness perspectives.

For uniform-height building arrays, in terms of the ensemble-average surface temperature drop, cool roofs & walls (CR&W) yield the best cooling effect (0.83–1.52 ℃) under two street orientations, while cool roofs (CR) show the worst (0.47–0.50 ℃). However, when the cost of cool coatings (i.e., area of cool-coated surface) is taken into account, the results are opposite. CR achieves the highest average surface temperature drop per unit of cool-coated surface (7.91×10^{-4}–8.26×10^{-4} °C/m^2), much greater than CR&W. It is worth noting that east-west walls show a greater temperature drop than north-south walls under cool coatings (Fig. 9(a)), especially in N-S oriented building arrays. Consequently, when the cooling effect is prioritized, cool coatings should be used on the entire building envelope (CR&W); nevertheless, when coating costs are given equal priority to the cooling effect, applying cool coatings only to roofs and east-west walls (CR&EWW) can be a good trade-off between effect and costs. Moreover, it is direct sunlit zones that undertake the dominant surface temperature drop of east-west walls (Fig. 5). Li et al. (2024) also confirmed that cool-coating 50% and 25% of walls achieves comparable cooling effects to entirely-cool-coated walls. Therefore, to further save cool coating costs and optimize cooling intensity, east-west walls can be partially cool-coated according to sunlit zones, particularly in compact high-rise urban areas.

Moreover, for varied-height building arrays, our results demonstrate that adding cool coatings to low-rise building walls provides only about half the cooling effect of using cool coatings on high-rise building walls (Fig. 10(a)). The cooling effect of cool low-rise walls would further decrease if low-rise buildings were shaded more extensively by high-rise buildings than is the case in this study. Therefore, applying cool coatings on roofs and only high-rise building walls (CR&HW) is a cost-effective configuration for varied-height building arrays. This strategy enhances cooling magnitude and intensity for high-rise buildings relative to CR&W, and for low-rise buildings relative to CR.

4. Limitations and future work

This study provides valuable insights into the effects of cool coatings on urban microclimate through CFD simulations. Despite these contributions, several limitations remain and require further research.

First, the simulations employ the steady RANS approach and examine only three representative local times (LT08, LT12, and LT16) on a summer day, which may not fully reveal the dynamic impacts of cool coatings over diurnal and seasonal cycles. Previous studies indicate that cool coatings can provide nighttime cooling (Lu et al., 2023; Sinsel et al., 2021b; Zhou et al., 2020). Therefore, dedicated research using unsteady simulations and systematic nocturnal analysis is required to investigate their performance across diurnal and seasonal cycles.

Second, this study focuses on idealized urban building arrays with typical street orientations (N-S and E-W) and building height layouts (uniform height and alternate height variability) to highlight the effects of street orientation and height variability. However, alternative street orientations and height layouts not considered in this study may lead to different results. Moreover, real-world urban morphologies are often more complex and diverse, including irregular street layouts, diverse building configurations, varying street widths, water bodies, and vegetation. Further investigations are needed to examine a wider range of urban morphological parameters and meteorological conditions. Particularly, combining cool coatings, water bodies, and vegetation is a promising strategy for urban cooling and deserves in-depth research. This study provides a useful CFD modeling prototype and evaluation methods for future work in more complex urban environments.

Third, this study assumes identical cool coating materials applied to different surfaces (cool roofs, cool walls, and their combinations), without considering variations in material properties (e.g., infrared reflectivity and emissivity), aging, and maintenance. These factors may influence the actual performance of cool coatings in real-world cities. Besides, coating cost is currently quantified solely by coating area. In practice, however, additional factors such as wind speed at different heights, coating degradation, and maintenance would impact both cooling effect and coating cost. Future research should include the above factors and provide more comprehensive cost considerations.

Fourth, our analysis centers on building surface temperature and pedestrian-level microclimate in summer, and does not involve the broader impacts of cool coatings, such as thermal comfort, building energy use, and known adverse effects. Although cool coatings can lower air-surface temperatures, they may elevate mean radiant temperature through increasing reflected solar radiation, worsening outdoor thermal comfort (Elmagri et al., 2024; Lai et al., 2019). Besides, cool coatings can also increase building heating loads in cold climate zones or winter (He et al., 2020; Xu et al., 2024c), and high-reflective surfaces may cause glare or visual discomfort, posing safety concerns (Liu & Morawska, 2020). Therefore, there is a need for future work to analyze thermal comfort and building energy use and to evaluate potential adverse effects.

To achieve these research plans, we will further optimize CFD methods coupling turbulence, radiation, and heat transfer models in the pursuit of high prediction precision and robustness. We have conducted multiple sets of scaled outdoor experiments in the SOMUCH platform in a humid subtropical zone, which examined albedo, airflow, air-surface temperatures, and heat storage flux in various 3D urban building arrays with and without cool coatings (Hang et al., 2025; Lu et al., 2023). Similar experiments in the temperate zone are in preparation. They can offer high-quality and high-resolution experimental data for model validation (Chen et al., 2025), supporting our future CFD simulations.

5. Conclusion

This study employs CFD simulations to investigate the synergetic cooling effects of cool coating configuration, street orientation, and height variability on building envelopes and pedestrian-level microclimate in 3D open high-rise urban areas under solar radiation heating (LT08, LT12, and LT16). Three types of full-scale building arrays are designed by varying street orientation (N-S vs. E-W) and building height layout (UH vs. VH). Cool coating configurations include five combinations: no cool coatings, cool roofs, cool roofs & all walls, cool roofs & only east-west walls, and cool roofs & only high-rise walls. Pedestrian-level wind velocity and air temperature, as well as building surface temperature, across various cases are compared, and the effectiveness of cool coatings in modifying these variables is evaluated. Novel indices, i.e., cooling magnitude and cooling intensity, are proposed to evaluate the cooling performance of cool coatings on buildings. The former quantifies the ensemble-average surface temperature drop, while the latter measures the average surface temperature drop per unit of cool-coated surface area. The key findings are summarized as follows:

(1) In terms of T_{sur}, the highest-temperature region occurs on roofs at noon and on direct sunlit zones of east-west walls in the morning and afternoon. Cool

coatings demonstrate the most significant cooling effects on direct sunlit zones at each time, while they hardly cool shaded zones. Their time-averaged cooling effect peaks at roofs (4.21–5.00 ℃), followed by east-west walls (0.49–1.51 ℃), and finally north-south walls (0.19–0.38 ℃). Street orientation and height variability significantly change the size of direct sunlit and shaded zones on walls at low solar altitudes, thereby affecting T_{sur} and the cooling effect of cool coatings.

(2) Regarding pedestrian-level microclimate, cooling coatings slightly decrease air temperature (< 0.27 ℃), with negligible effects on wind velocity ratio (variation < 0.06). CR&W has a greater effect on pedestrian-level microclimate than CR.

(3) Concerning cooling magnitude, CR&W, CR&EWW, and CR&HW exhibit superior cooling performance compared to CR. However, when considering the cost of cool coatings, CR, CR&EWW, and CR&HW outperform CR&W in cooling intensity. Thus, CR&EWW can be a good trade-off between cooling effect and coating costs for uniform-height building arrays; CR&HW is a cost-effective strategy for varied-height building arrays, as it enhances cooling magnitude and intensity for high-rise buildings relative to CR&W, and for low-rise buildings relative to CR.

(4) N-S street orientation shows consistently greater cooling magnitude and generally higher cooling intensity than E-W street orientation, demonstrating its superior cooling performance with cool coatings. Compared to uniform-

height building arrays, low-rise buildings show enhanced cooling intensity under CR but reduced cooling intensity under CR&W; high-rise buildings exhibit reduced cooling intensity under both CR and CR&W.

This study provides a quantitative analysis of cool coatings' performance across various coating configurations and urban morphologies, offering scientific evidence and useful design suggestions for the application of cool coatings. The results demonstrate that rational urban design with adequate cool coating configurations can effectively decrease air-surface temperatures, thus mitigating the UHI effect and reducing building energy consumption.

References

Abd Elraouf, R., Elmokadem, A., Megahed, N., Abo Eleinen, O., & Eltarabily, S. (2022). The impact of urban geometry on outdoor thermal comfort in a hot-humid climate. *Building and Environment*, *225*, 109632. https://doi.org/10.1016/j.buildenv.2022.109632

Adelia, A. S., Yuan, C., Liu, L., & Shan, R. Q. (2019). Effects of urban morphology on anthropogenic heat dispersion in tropical high-density residential areas. *Energy and Buildings*, *186*, 368–383. https://doi.org/10.1016/j.enbuild.2019.01.026

Alfonsi, G. (2009). Reynolds-Averaged Navier–Stokes Equations for Turbulence Modeling. *Applied Mechanics Reviews*, *62*(4), 040802. https://doi.org/10.1115/1.3124648

ANSYS Inc.. (2023). ANSYS Fluent Theory Guide. Release 2023R1.

Antoniou, N., Montazeri, H., Neophytou, M., & Blocken, B. (2019). CFD simulation of urban microclimate: Validation using high-resolution field measurements. *Science of The Total Environment*, *695*, 133743. https://doi.org/10.1016/j.scitotenv.2019.133743

Barbosa, I. S. O., Santos, R. J., Dias, M. M., Faria, J. L., & Silva, C. G. (2023). Radiation Models for Computational Fluid Dynamics Simulations of Photocatalytic Reactors. *Chemical Engineering & Technology*, *46*(6), 1059–1077. https://doi.org/10.1002/ceat.202200551

Blocken, B. (2015). Computational Fluid Dynamics for urban physics: Importance, scales, possibilities, limitations and ten tips and tricks towards accurate and reliable simulations. *Building and Environment*, *91*, 219–245. https://doi.org/10.1016/j.buildenv.2015.02.015

Blocken, B. (2018). LES over RANS in building simulation for outdoor and indoor applications: A foregone conclusion? *Building Simulation*, *11*(5), 821–870. https://doi.org/10.1007/s12273-018-0459-3

Blocken, B., Stathopoulos, T., & Carmeliet, J. (2007). CFD simulation of the atmospheric boundary layer: Wall function problems. *Atmospheric Environment*, *41*(2), 238–252. https://doi.org/10.1016/j.atmosenv.2006.08.019

Bottillo, S., De Lieto Vollaro, A., Galli, G., & Vallati, A. (2014). CFD modeling of the impact of solar radiation in a tridimensional urban canyon at different wind conditions. *Solar Energy*, *102*, 212–222. https://doi.org/10.

1016/j.solener.2014.01.029

Buratti, C., Palladino, D., Moretti, E., & Palma, R. D. (2018). Development and optimization of a new ventilated brick wall: CFD analysis and experimental validation. *Energy and Buildings*, *168*, 284–297. https://doi.org/10.1016/j.enbuild.2018.03.041

Cai, W., Zhang, C., Suen, H. P., Ai, S., Bai, Y., Bao, J., Chen, B., Cheng, L., Cui, X., Dai, H., Di, Q., Dong, W., Dou, D., Fan, W., Fan, X., Gao, T., Geng, Y., Guan, D., Guo, Y., … Gong, P. (2021). The 2020 China report of the Lancet Countdown on health and climate change. *The Lancet Public Health*, *6*(1), e64–e81. https://doi.org/10.1016/S2468-2667(20)30256-5

Cao, M., Rosado, P., Lin, Z., Levinson, R., & Millstein, D. (2015). Cool roofs in Guangzhou, China: Outdoor air temperature reductions during heat waves and typical summer conditions. *Environmental Science & Technology*, *49*(24), 14672–14679. https://doi.org/10.1021/acs.est.5b04886

Chang, Y., Van Strien, M. J., Zohner, C. M., Ghazoul, J., & Kleinschroth, F. (2024). Effects of climate, socioeconomic development, and greening governance on enhanced greenness under urban densification. *Resources, Conservation and Recycling*, *206*, 107624. https://doi.org/10.1016/j.resconrec.2024.107624

Chen, G., Mei, S.-J., Hang, J., Li, Q., & Wang, X. (2025). URANS simulations of urban microclimates: Validated by scaled outdoor experiments. *Buil* *ding and Environment*, *272*, 112691. https://doi.org/10.1016/j.buildenv.2025.112691

Chen, G., Wang, D., Wang, Q., Li, Y., Wang, X., Hang, J., Gao, P., Ou, C., & Wang, K. (2020). Scaled outdoor experimental studies of urban thermal environment in street canyon models with various aspect ratios and thermal storage. *Science of the total environment*, 726, 138147. https://doi.org/10.1016/j.scitotenv.2020.138147

Chen, L., & Frauenfeld, O. W. (2016). Impacts of urbanization on future climate in China. *Climate Dynamics*, *47*(1–2), 345–357. https://doi.org/10.1007/s00382-015-2840-6

Chen, L., Hang, J., Sandberg, M., Claesson, L., Di Sabatino, S., & Wigo, H. (2017). The impacts of building height variations and building packing densities on flow adjustment and city breathability in idealized urban models. *Building and Environment*, *118*, 344–361. https://doi.org/10.1016/j.buildenv.2017.03.042

Chen, R., & You, X. (2020). Reduction of urban heat island and associated greenhouse gas emissions. *Mitigation and Adaptation Strategies for Global Change*, *25*(4), 689–711. https://doi.org/10.1007/s11027-019-09886-1

Chen, Y., Yang, J., Yu, W., Ren, J., Xiao, X., & Xia, J. C. (2023). Relationship between urban spatial form and seasonal land surface temperature under different grid scales. *Sustainable Cities and Society*, *89*, 104374. https://doi.org/10.1016/j.scs.2022.104374

Dimoudi, A., Zoras, S., Kantzioura, A., Stogiannou, X., Kosmopoulos, P., & Pallas, C. (2014). Use of cool materials and other bioclimatic interventions in outdoor places in order to mitigate the urban heat island in a medium size city in Greece. *Sustainable Cities and Society*, *13*, 89–96. https://doi.org/10.1016/j.scs.2014.04.003

Donthu, E. V. S. K. K., Long, Y. P., Wan, M. P., Zhou, M., & Ng, B. F. (2024a). Dynamics of cool surface performance on urban microclimate: A full-scale experimental study in Singapore. *Sustainable Cities and Society*, *102*, 105218. https://doi.org/10.1016/j.scs.2024.105218

Donthu, E. V. S. K. K., Kyriakodis, G.-E., Zhang, X., Long, Y. P., Wan, M. P., & Bozonnet, E. (2024b). Simulation advances with EnviBatE- A case study on urban heat island mitigation in Singapore. *Building and Environment*, *258*, 111580. https://doi.org/10.1016/j.buildenv.2024.111580

Elmagri, H., Kamel, T. M., & Ozer, H. (2024). Assessment of the effectiveness of cool pavements on outdoor thermal environment in urban areas. *Building and Environmen*t, *266*, 112095. https://doi.org/10.1016/j.buildenv.2024.112095

Elnabawi, M. H., Hamza, N., & Raveendran, R. (2023). 'Super cool roofs': Mitigating the UHI effect and enhancing urban thermal comfort with high albedo-coated roofs. *Results in Engineering*, *19*, 101269. https://doi.org/10.1016/j.rineng.2023.101269

Fabiani, C., & Pisello, A. L. (2021). Cool Materials for Passive Cooling in Bu ildings. In M. Palme & A. Salvati (Eds.), *Urban Microclimate Modelling for Comfort and Energy Studies* (pp. 505–537). Springer International Publishing. https://doi.org/10.1007/978-3-030-65421-4_24

Franke, J., Hirsch, C., Jensen, A. G., Krüs, H. W., Schatzmann, M., Westbury, P. S., Miles, S. D., Wisse, J. A., & Wright, N. G. (2004). Recommendations on the use of CFD in wind engineering. *Proceedings of the International Conference on Urban Wind Engineering and Building Aerodynamics*.

Georgakis, Ch., Zoras, S., & Santamouris, M. (2014). Studying the effect of "cool" coatings in street urban canyons and its potential as a heat island mitigation technique. *Sustainable Cities and Society*, *13*, 20–31. https://doi.org/10.1016/j.scs.2014.04.002

Gromke, C., Blocken, B., Janssen, W., Merema, B., van Hooff, T., & Timmermans, H. (2015). CFD analysis of transpirational cooling by vegetation: Case study for specific meteorological conditions during a heat wave in Arnhem, Netherlands. *Building and Environment*, *83*, 11–26. https://doi.org/10.1016/j.buildenv.2014.04.022

Hang, J., Li, Q., Du, Y., Feng, J., Hua, J., & Zhao, B. (2024). Effects of arcade design on wind and thermal environment inside an idealized 2D urban canyon with realistic solar heating. *Building and Environment*, *254*, 111329. https://doi.org/10.1016/j.buildenv.2024.111329

Hang, J., Lu, M., Ren, L., Dong, H., Zhao, Y., & Zhao, N. (2025). Cooling p erformance of near-infrared and traditional high-reflective coatings under various coating modes and building area densities in 3D urban models: Scaled outdoor experiments. *Sustainable Cities and Society*, *121*, 106200. https://doi.org/10.1016/j.scs.2025.106200

Hang, J., Luo, Z., Sandberg, M., & Gong, J. (2013). Natural ventilation assess ment in typical open and semi-open urban environments under various wind directions. *Building and Environment*, *70*, 318–333. https://doi.org/10.1016/j.buildenv.2013.09.002

He, Y., Yu, H., Ozaki, A., & Dong, N. (2020). Thermal and energy performan ce of green roof and cool roof: A comparison study in Shanghai area. *Journal of Cleaner Production*, *267*, 122205. https://doi.org/10.1016/j.jclepro.2020.122205

Hu, N., Wang, G., Ma, Z., Ren, Z., Zhao, M., & Meng, J. (2023). The coolin g effects of urban waterbodies and their driving forces in China. *Ecological Indicators*, *156*, 111200. https://doi.org/10.1016/j.ecolind.2023.111200

Huo, H., Chen, F., Geng, X., Tao, J., Liu, Z., Zhang, W., & Leng, P. (2021). Simulation of the Urban Space Thermal Environment Based on Computa tional Fluid Dynamics: A Comprehensive Review. *Sensors*, *21*(20), Articl e 20. https://doi.org/10.3390/s21206898

Kolokotsa, D. – D., Giannariakis, G., Gobakis, K., Giannarakis, G., Synnefa, A., & Santamouris, M. (2018). Cool roofs and cool pavements applicati on in Acharnes, Greece. *Sustainable Cities and Society*, *37*, 466–474. htt ps://doi.org/10.1016/j.scs.2017.11.035

Krayenhoff, E. S., Broadbent, A. M., Zhao, L., Georgescu, M., Middel, A., Vogt, J. A., Martilli, A., Sailor, D. J., & Erell, E. (2021). Cooling hot cities: A systematic and critical review of the numerical modelling literature. *Environmental Research Letters*, *16*(5), 053007. https://doi.org/10.1088/1748-9326/abdcf1

Lai, D., Liu, W., Gan, T., Liu, K., & Chen, Q. (2019). A review of mitigating strategies to improve the thermal environment and thermal comfort in urban outdoor spaces. *Science of The Total Environment*, *661*, 337–353. https://doi.org/10.1016/j.scitotenv.2019.01.062

Li, D. (2025). Bridging the Gap Between Applied Meteorology and Climate Science: A White Roof Example. *ARC Geophysical Research*, *1*(1), Article 1. https://doi.org/10.5149/ARC-GR.1418

Li, Q., Zhang, X., & Hang, J. (2024). Numerical investigations of cool coatings on building envelopes for urban heat mitigation with various street aspect ratios. *Sustainable Cities and Society*, *107*, 105410. https://doi.org/10.1016/j.scs.2024.105410

Li, R., Liu, J., Chen, X., Zhang, W., Lei, T., Chen, J., Xia, Y., & Bantserova, O. L. (2025). Transient thermal comfort during summer in air-conditioned indoor and naturally ventilated transitional spaces − A field study in Zhengzhou, China. *Energy and Buildings*, 328, 115122. https://doi.org/10.1016/j.enbuild.2024.115122

Li, X., Zhou, Y., Yu, S., Jia, G., Li, H., & Li, W. (2019). Urban heat island impacts on building energy consumption: A review of approaches and findings. *Energy*, *174*, 407–419. https://doi.org/10.1016/j.energy.2019.02.183

Lin, Y., Chen, G., Chen, T., Luo, Z., Yuan, C., Gao, P., & Hang, J. (2019). The influence of advertisement boards, street and source layouts on CO dispersion and building intake fraction in three-dimensional urban-like models. *Building and Environment*, *150*, 297–321. https://doi.org/10.1016/j.buildenv.2019.01.012

Liu, J., & Niu, J. (2016). CFD simulation of the wind environment around an isolated high-rise building: An evaluation of SRANS, LES and DES models. *Building and Environment*, *96*, 91–106. https://doi.org/10.1016/j.buildenv.2015.11.007

Liu, N., & Morawska, L. (2020). Modeling the urban heat island mitigation effect of cool coatings in realistic urban morphology. *Journal of Cleaner Production*, *264*, 121560. https://doi.org/10.1016/j.jclepro.2020.121560

Liu, S., Xu, L., Chen, B., Deng, Z., Li, P., Zhao, R., & Chen, Q. (2025). Recent progress in optimization of RANS turbulence models for accurate urban airflow and contaminant dispersion simulations. *Sustainable Cities and Society*, *125*, 106336. https://doi.org/10.1016/j.scs.2025.106336

Liu, S., Yang, X., Yang, H., Gao, P., Hang, J., & Wang, Q. (2021). Numerical investigation of solar impacts on canyon vortices and its dynamical generation mechanism. *Urban Climate*, *39*, 100978. https://doi.org/10.1016/j.u clim.2021.100978

Liu, X., Chen, X., & Shahrestani, M. (2020). Optimization of insulation thickness of external walls of residential buildings in hot summer and cold winter zone of China. *Sustainability*, *12*(4), 1574. https://doi.org/10.3390/su12041574

Liu, Y., Chu, C., Zhang, R., Chen, S., Xu, C., Zhao, D., Meng, C., Ju, M., & Cao, Z. (2024). Impacts of high-albedo urban surfaces on outdoor thermal environment across morphological contexts: A case of Tianjin, China. *Sustainable Cities and Society*, *100*, 105038. https://doi.org/10.1016/j.scs.2023.105038

Lu, M., Zeng, L., Li, Q., Hang, J., Hua, J., Wang, X., & Wang, W. (2023). Quantifying cooling benefits of cool roofs and walls applied in building clusters by scaled outdoor experiments. *Sustainable Cities and Society*, *97*, 104741. https://doi.org/10.1016/j.scs.2023.104741

Mandal, J., Fu, Y., Overvig, A. C., Jia, M., Sun, K., Shi, N. N., Zhou, H., Xiao, X., Yu, N., & Yang, Y. (2018). Hierarchically porous polymer coatings for highly efficient passive daytime radiative cooling. *Science*, *362*(6412), 315–319. https://doi.org/10.1126/science.aat9513

Matthews, T. K. R., Wilby, R. L., & Murphy, C. (2017). Communicating the deadly consequences of global warming for human heat stress. *Proceedings of the National Academy of Sciences*, *114*(15), 3861–3866. https://doi.org/10.1073/pnas.1617526114

Morini, E., Castellani, B., De Ciantis, S., Anderini, E., & Rossi, F. (2018). Planning for cooler urban canyons: Comparative analysis of the influence of façades reflective properties on urban canyon thermal behavior. *Solar Energy*, *162*, 14–27. https://doi.org/10.1016/j.solener.2017.12.064

National Centers for Environmental Information (NCEI). (accessed on 25 May, 2025) https://www.ncei.noaa.gov/

Park, K., & Baik, J.-J. (2024). Nonlinear changes in urban heat island intensity, urban breeze intensity, and urban air pollutant concentration with roof albedo. *Scientific Reports*, *14*(1), 24911. https://doi.org/10.1038/s41598-024-76935-4

Popiel, C. O., Wojtkowiak, J., & Biernacka, B. (2001). Measurements of temperature distribution in ground. *Experimental Thermal and Fluid Science*, *25*(5), 301–309. https://doi.org/10.1016/S0894-1777(01)00078-4

Qiao, Z., Wang, N., Chen, J., He, T., Xu, X., Liu, L., Sun, Z., & Han, D. (2023). Urbanization accelerates urban warming by changing wind speed: Evidence from China based on 2421 meteorological stations from 1978 to 2017. *Environmental Impact Assessment Review*, *102*, 107189. https://doi.org/10.1016/j.eiar.2023.107189

Rao, Y., Zhang, S., Yang, K., Ma, Y., Wang, W., & Niu, L. (2024). Scale Differences and Gradient Effects of Local Climate Zone Spatial Pattern on Urban Heat Island Impact—A Case in Guangzhou's Core Area. *Sustainability*, *16*(15), 6656. https://doi.org/10.3390/su16156656

Reed, K., & Sun, F. (2023). Investigating the potential for cool roofs to mitigate urban heat in the Kansas City metropolitan area. *Climate Dynamics*, *60*(1), 461–475. https://doi.org/10.1007/s00382-022-06296-z

Ren, Z., Wang, C., Guo, Y., Hong, S., Zhang, P., Ma, Z., Hong, W., Wang, X., Geng, R., & Meng, F. (2024). The cooling capacity of urban vegetation and its driving force under extreme hot weather: A comparative study between dry-hot and humid-hot cities. *Building and Environment*, *263*, 111901. https://doi.org/10.1016/j.buildenv.2024.111901

Roache, P. J. (1997). Quantification of uncertainty in computational fluid dynamics. *Annual Review of Fluid Mechanics*, *29*(1), 123–160. https://doi.org/10.1146/annurev.fluid.29.1.123

Santamouris, M., Synnefa, A., & Karlessi, T. (2011). Using advanced cool materials in the urban built environment to mitigate heat islands and improve thermal comfort conditions. *Solar Energy*, *85*(12), 3085–3102. https://doi.org/10.1016/j.solener.2010.12.023

Sazhin, S. S., Sazhina, E. M., Faltsi-Saravelou, O., & Wild, P. (1996). The P-1 model for thermal radiation transfer: Advantages and limitations. *Fuel*, *75*(3), 289–294. https://doi.org/10.1016/0016-2361(95)00269-3

Sen, S., & Khazanovich, L. (2021). Limited application of reflective surfaces can mitigate urban heat pollution. *Nature Communications*, *12*(1), 3491. https://doi.org/10.1038/s41467-021-23634-7

Sha, C., Wang, X., Lin, Y., Fan, Y., Chen, X., & Hang, J. (2018). The impact of urban open space and 'lift-up' building design on building intake fraction and daily pollutant exposure in idealized urban models. *Science of The Total Environment*, *633*, 1314–1328. https://doi.org/10.1016/j.scitotenv.2018.03.194

Sinsel, T., Simon, H., Broadbent, A. M., Bruse, M., & Heusinger, J. (2021a). Modeling impacts of super cool roofs on air temperature at pedestrian level in mesoscale and microscale climate models. *Urban Climate*, *40*, 101001. https://doi.org/10.1016/j.uclim.2021.101001

Sinsel, T., Simon, H., Broadbent, A. M., Bruse, M., & Heusinger, J. (2021b). Modeling the outdoor cooling impact of highly radiative "super cool" materials applied on roofs. *Urban Climate*, *38*, 100898. https://doi.org/10.1016/j.uclim.2021.100898

Sun, R., & Chen, L. (2012). How can urban water bodies be designed for climate adaptation? *Landscape and Urban Planning*, *105*(1–2), 27–33. https://doi.org/10.1016/j.landurbplan.2011.11.018

Taleghani, M., Swan, W., Johansson, E., & Ji, Y. (2021). Urban cooling: Which façade orientation has the most impact on a microclimate? *Sustainable Cities and Society*, *64*, 102547. https://doi.org/10.1016/j.scs.2020.102547

Tominaga, Y., Mochida, A., Yoshie, R., Kataoka, H., Nozu, T., Yoshikawa, M., & Shirasawa, T. (2008). AIJ guidelines for practical applications of CFD to pedestrian wind environment around buildings. *Journal of Wind Engineering and Industrial Aerodynamics*, *96*(10–11), 1749–1761. https://doi.

org/10.1016/j.jweia.2008.02.058

Toparlar, Y., Blocken, B., Vos, P., Van Heijst, G. J. F., Janssen, W. D., Van Hooff, T., Montazeri, H., & Timmermans, H. J. P. (2015). CFD simulation and validation of urban microclimate: A case study for Bergpolder Zuid, Rotterdam. *Building and Environment*, *83*, 79–90. https://doi.org/10.1016/j.buildenv.2014.08.004

United Nations, World Urbanization Prospects: The 2018 Revision, United Nations, New York, 2018.

Wang, W., Yang, T., Li, Y., & Ikegaya, N. (2025). Comparing RANS- and LES-based statistical methods for determining low-occurrence strong wind speeds in an actual urban area. *Building and Environment*, *269*, 112464. https://doi.org/10.1016/j.buildenv.2024.112464

Wang, X., Liu, G., Zhang, N., Liu, H., Tang, X., Lyu, M., & Meng, H. (2023). Effects of cooling roofs on mitigating the urban heat island and human thermal stress in the Pearl River Delta, China. *Building and Environment*, *245*, 110880. https://doi.org/10.1016/j.buildenv.2023.110880

WMO. (1996). Guide to meteorological instruments and methods of observation.

Xiang, X., Zhai, Z., Fan, C., Ding, Y., Ye, L., & Li, J. (2024). Modelling future land use land cover changes and their impacts on urban heat island intensity in Guangzhou, China. *Journal of Environmental Management*, *366*, 121787. https://doi.org/10.1016/j.jenvman.2024.121787

Xu, F., Tian, D., Gao, Z., & Zhang, J. J. (2024a). The effects of cool material s, façade orientation, and morphological parameters on energy consumption at the residential neighborhood scale. *Building Simulation*, *17*(4), 525–542. https://doi.org/10.1007/s12273-023-1096-z

Xu, F., Wang, H., Tian, D., Gao, Z., & Zhang, J. (2024b). Factors affecting the daytime cooling effect of cool materials: A case study combining experiment and simulation. *Building and Environment*, *250*, 111213. https://doi.org/10.1016/j.buildenv.2024.111213

Xu, F., Zhang, J., & Gao, Z. (2024c). A case study of the effect of building surface cool and super cool materials on residential neighbourhood energy consumption in Nanjing. *Renewable and Sustainable Energy Reviews*, *189*, 114027. https://doi.org/10.1016/j.rser.2023.114027

Xu, F., Zhang, J., & Gao, Z. (2023a). The effect of building surface cool and super cool materials on microclimate in typical residential neighborhoods in Nanjing. *Sustainable Cities and Society*, *98*, 104838. https://doi.org/10.1016/j.scs.2023.104838

Xu, F., Zhang, J. J., Gao, Z., Tian, D., & Wang, H. (2023b). Study on the energy-saving effects of radiative material properties and material coating ratios in residential neighborhoods with different morphologies. *Energy and Buildings*, *301*, 113718. https://doi.org/10.1016/j.enbuild.2023.113718

Zeeshan, M., & Ali, Z. (2022). The Potential of Cool Materials Towards Improving Thermal Comfort Conditions Inside Real-urban Hot-humid Microclimate. *Environment and Urbanization ASIA*, *13*(1), 56–72. https://doi.org/1

0.1177/09754253221083206

Zhang, J., Li, Y., Tao, W., Liu, J., Levinson, R., Mohegh, A., & Ban-Weiss, G. (2019). Investigating the Urban Air Quality Effects of Cool Walls and Cool Roofs in Southern California. *Environmental Science & Technology*, *53*(13), 7532–7542. https://doi.org/10.1021/acs.est.9b00626

Zhang, Y., Ou, C., Chen, L., Wu, L., Liu, J., Wang, X., Lin, H., Gao, P., & Hang, J. (2020). Numerical studies of passive and reactive pollutant disp ersion in high-density urban models with various building densities and height variations. *Building and Environment*, *177*, 106916. https://doi.org/ 10.1016/j.buildenv.2020.106916

Zhou, M., Long, Y., Zhang, X., Donthu, E. V. S. K. K., Ng, B. F., & Wan, M. P. (2020). Sensitivity Study of Weather Research and Forecasting Ph ysical Schemes and Evaluation of Cool Coating Effects in Singapore by Weather Research and Forecasting Coupled with Urban Canopy Model S imulations. *Journal of Geophysical Research: Atmospheres*, *125*(13), e20 19JD031191. https://doi.org/10.1029/2019JD031191

Zhu, S., & Chew, L. W. (2023). Flows across 3D urban street canyons: Reyno lds number independence revisited. In *Building Simulation Conference 20 23*. https://doi.org/10.26868/25222708.2023.1526

Zhu, Z., Zhou, D., Wang, Y., Ma, D., & Meng, X. (2021). Assessment of urba n surface and canopy cooling strategies in high-rise residential communit ies. *Journal of Cleaner Production*, *288*, 125599. https://doi.org/10.1016/j.

jclepro.2020.125599

Zinzi, M. (2016). Exploring the potentialities of cool facades to improve the thermal response of Mediterranean residential buildings. *Solar Energy*, *135*, 386–397. https://doi.org/10.1016/j.solener.2016.06.021

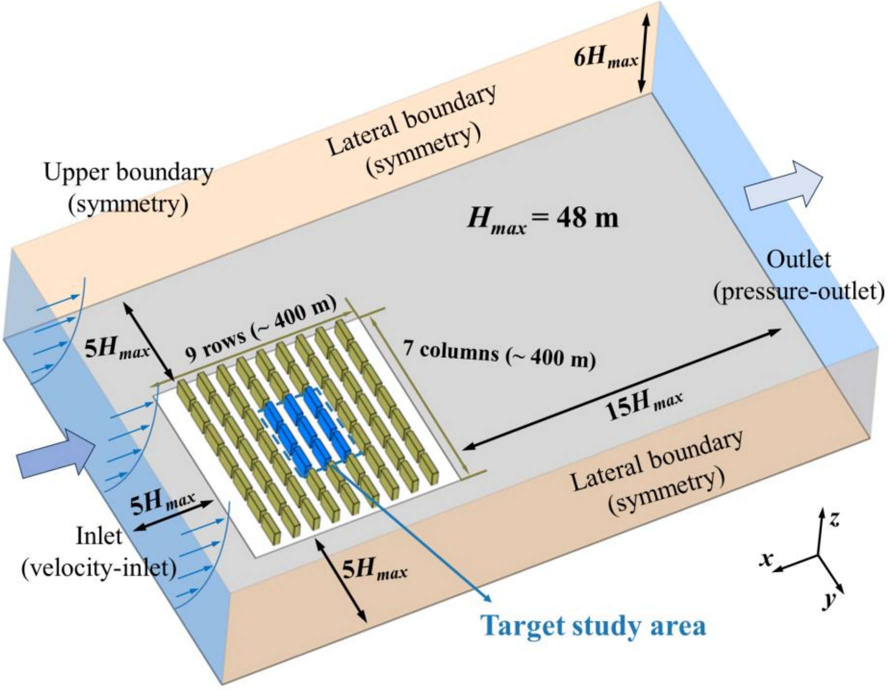
$6H_{max}$
Lateral boundary
(symmetry)
Upper boundary
(symmetry)
H_{max} = 48 m
Outlet
(pressure-outlet)
$5H_{max}$
9 rows (~ 400 m)
7 columns (~ 400 m)
$15H_{max}$
Lateral boundary
(symmetry)
$5H_{max}$
Inlet
(velocity-inlet)
$5H_{max}$
Target study area
z
x
y

(a)

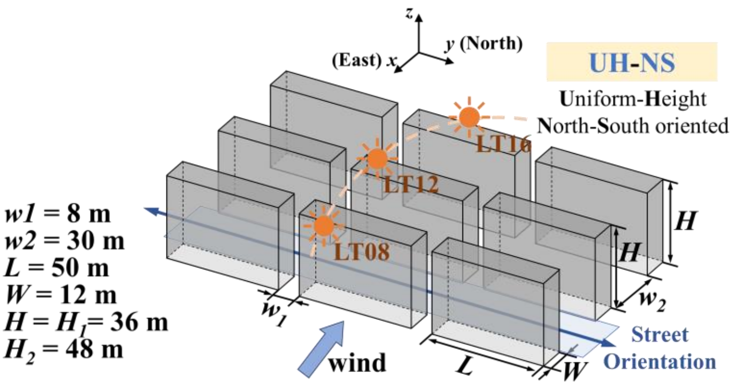
z
y (North)
(East) x
UH-NS
Uniform-Height
North-South oriented
LT16
LT12
LT08
$w1$ = 8 m
$w2$ = 30 m
L = 50 m
W = 12 m
$H = H_1$= 36 m
H_2 = 48 m
H
H
w_1
w_2
wind
L
W
Street
Orientation

(b)

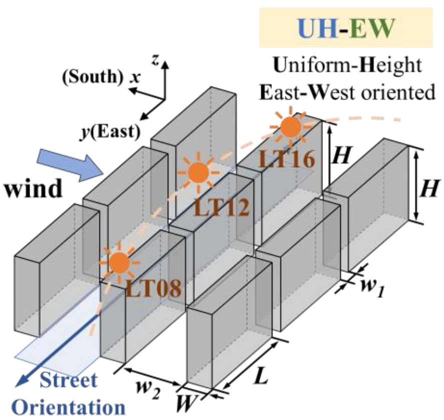
UH-EW
Uniform-Height
East-West oriented
(South) x
z
y(East)
wind
LT16
LT12
LT08
H
H
w_1
Street
Orientation
w_2
W
L

(c)

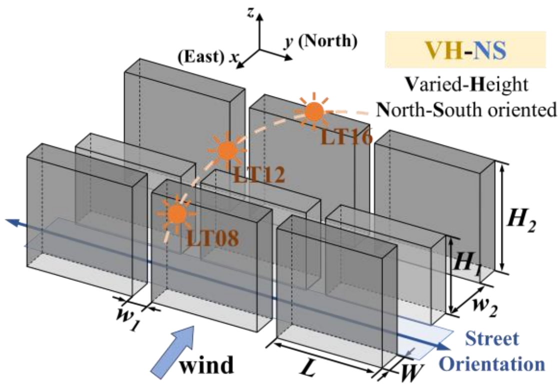
z
(East) x
y (North)
VH-NS
Varied-Height
North-South oriented
LT16
LT12
LT08
H_2
H_1
w_1
w_2
wind
L
W
Street
Orientation

(d)

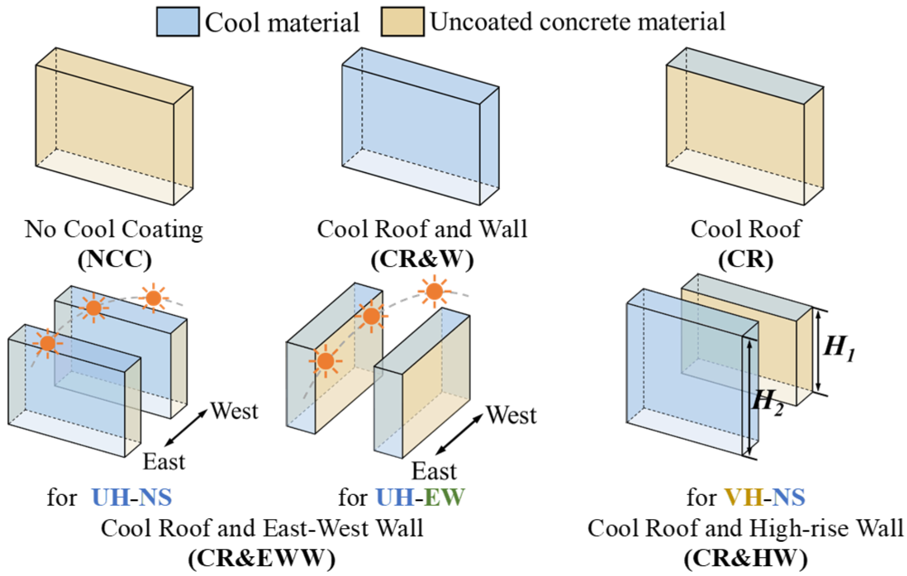

(e)

Fig. 1. Schematic diagrams of study cases: (a) computational domain; (b-d) three types of urban building array model—UH-NS model, UH-EW model, and VH-NS model; (e) five kinds of cool coating configurations: NCC, CR&W, and CR for all three models, CR&EWW for UH-NS and UH-EW models, and CR&HW for the VH-NS model.

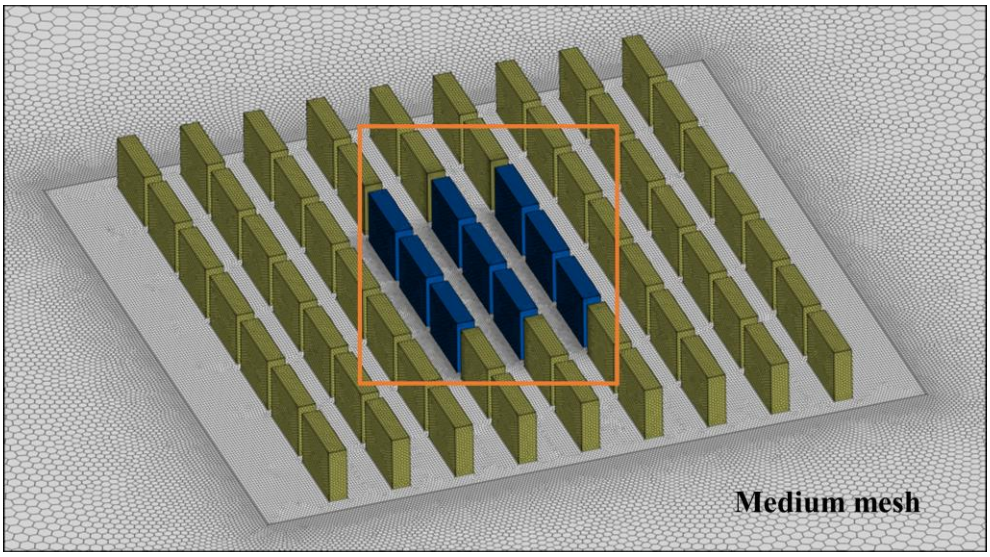

(a)

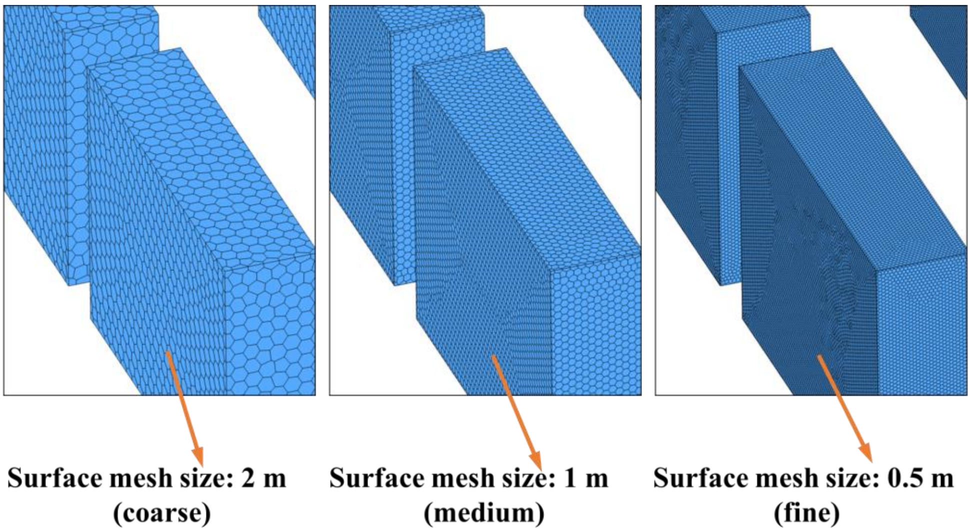

(b)

Fig. 2. Mesh arrangements for the UH-NS model without cool coatings at LT16.

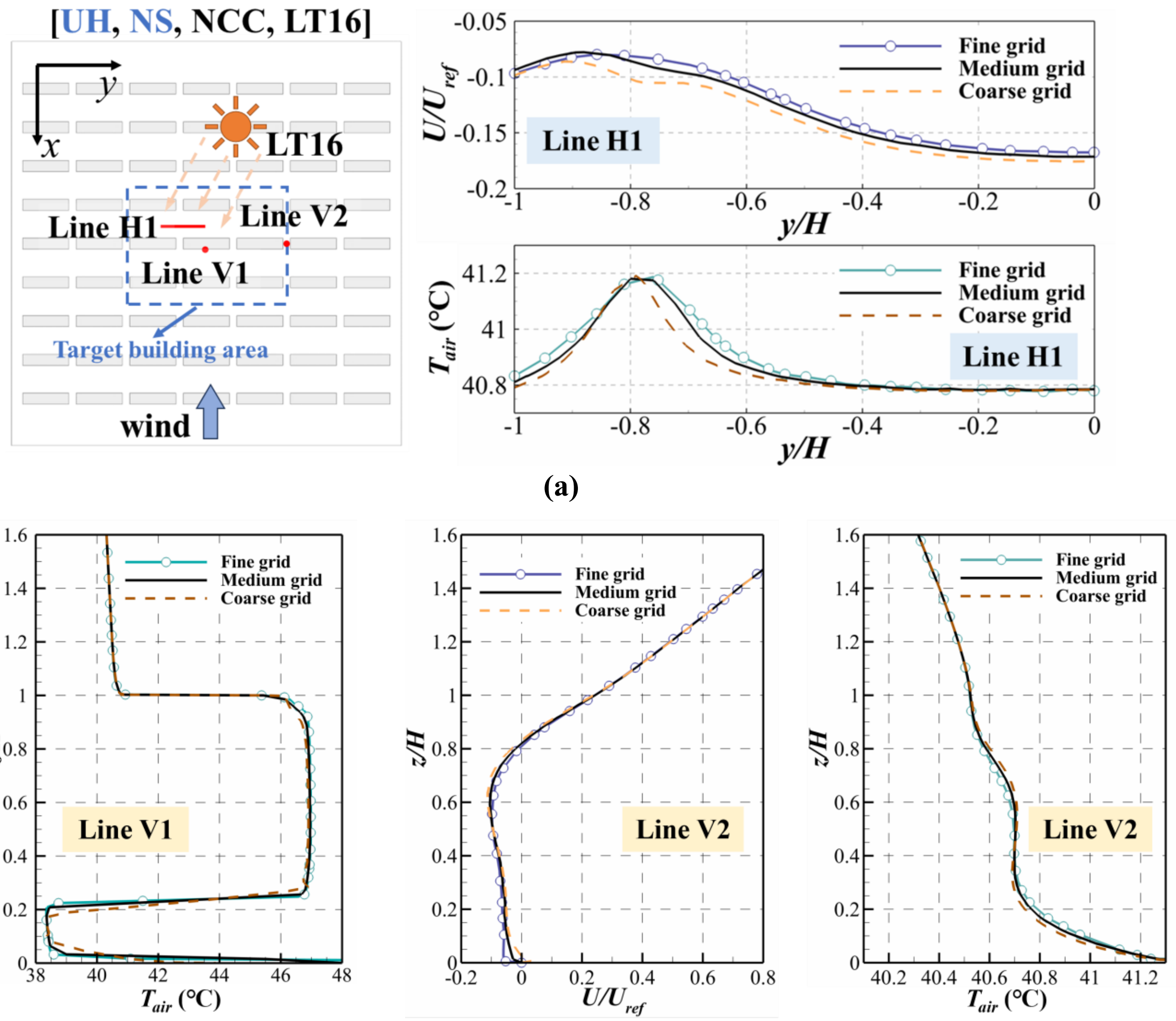

(b) **(c)**

Fig. 3. Results of the mesh sensitivity test among coarse, medium, and fine mesh arrangements: (a) U/U_{ref} and T_{air} at Line H1; (b) T_{air} at Line V1; (c) U/U_{ref} and T_{air} at Line V2.

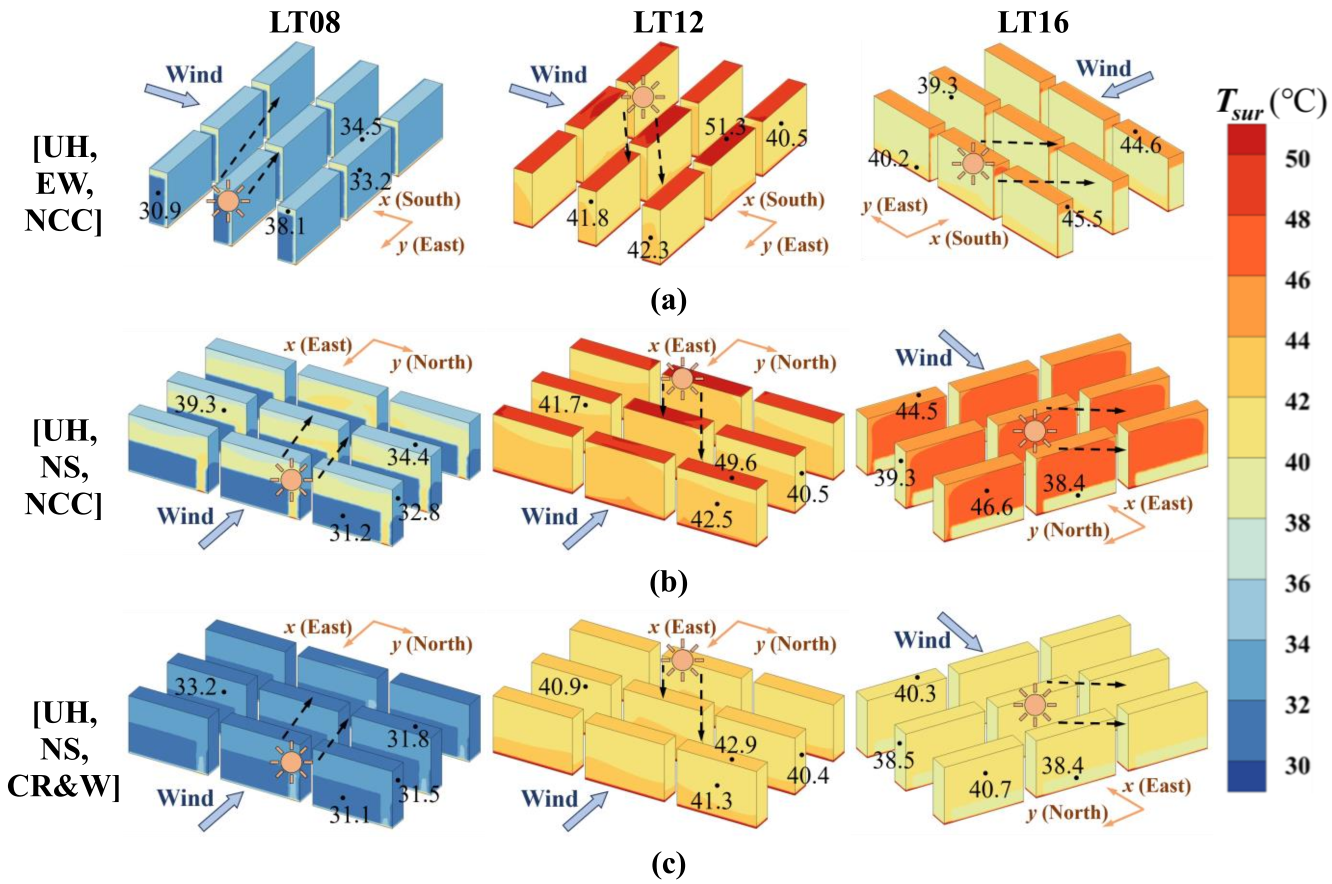

Fig. 4. Contour plots of building surface temperature (T_{sur}) for the (a) UH-EW and (b) UH-NS models under NCC and (c) for the UH-NS model under CR&W.

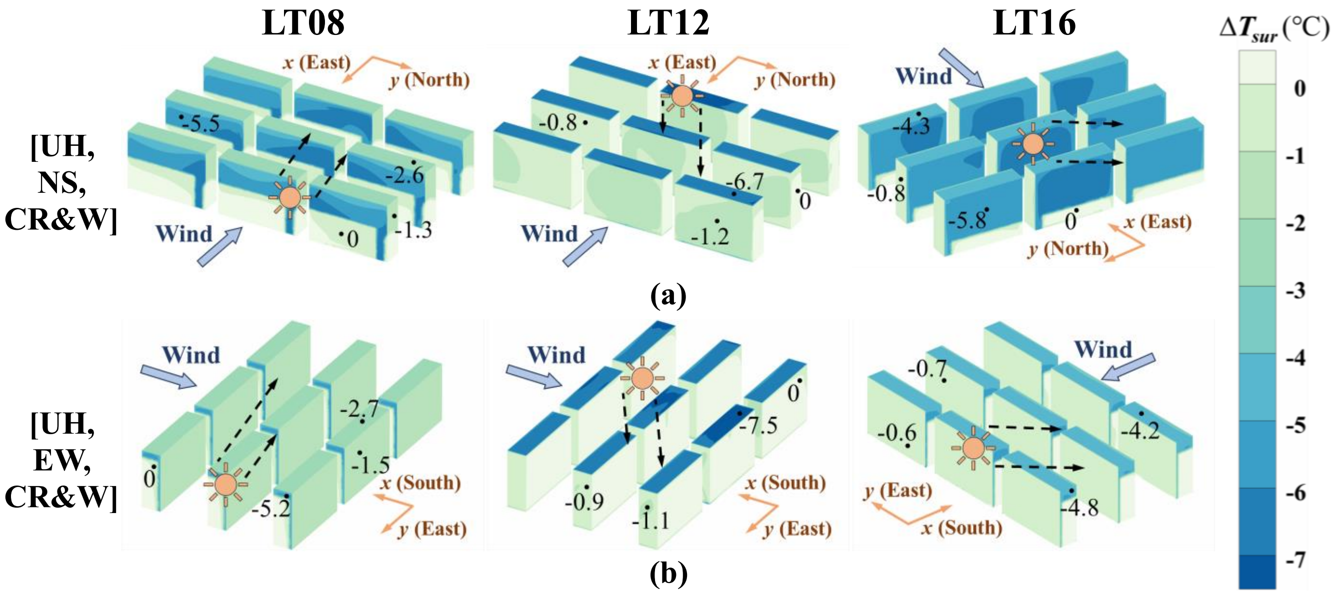

Fig. 5. Contour plots of building surface temperature drop (ΔT_{sur}) due to CR&W for the (a) UH-NS and (b) UH-EW models across different local times.

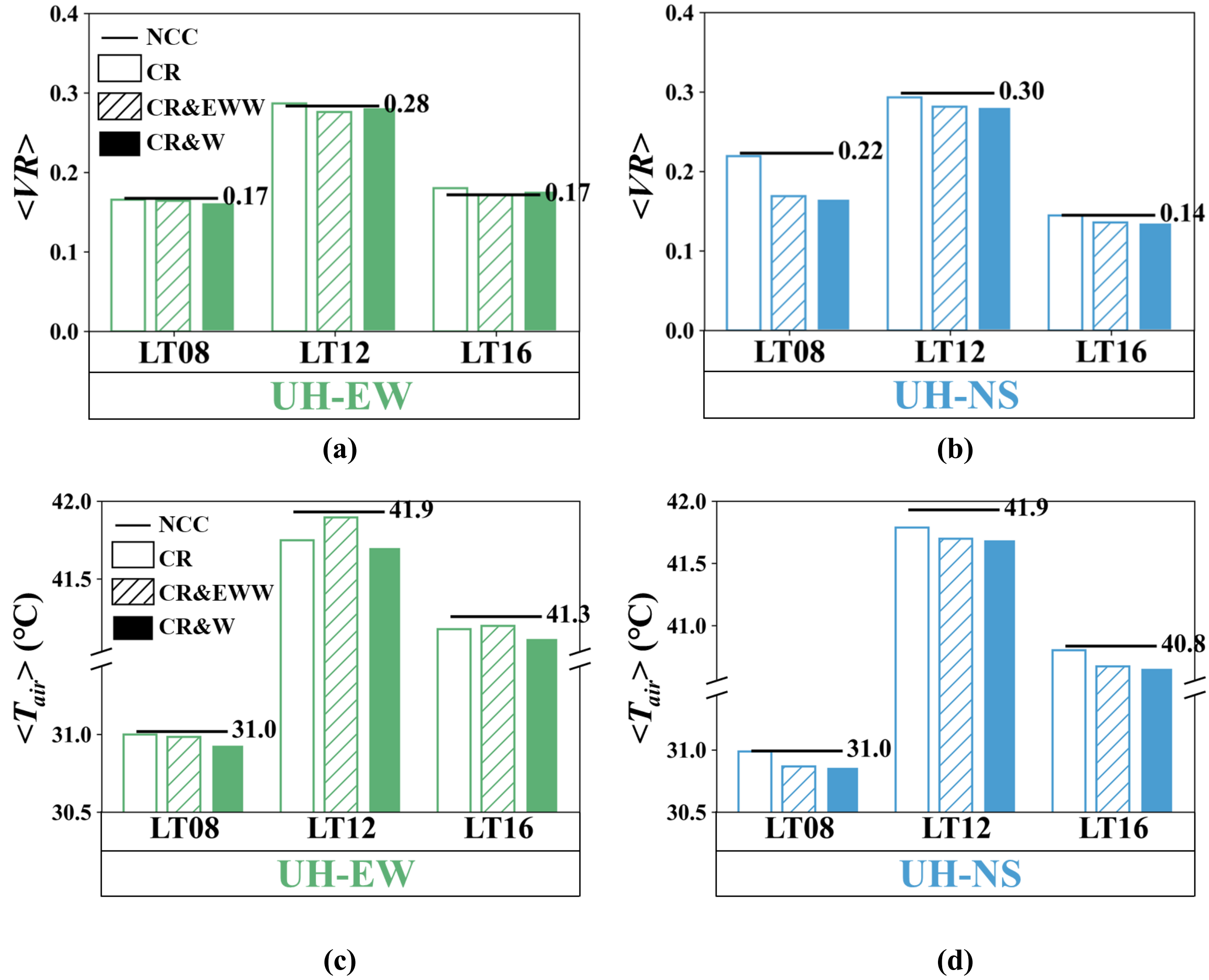

Fig. 6. Pedestrian-level area-averaged wind velocity ratio (<*VR*>) and air temperature (<T_{air}>) in the UH-EW and UH-NS models at different local times.

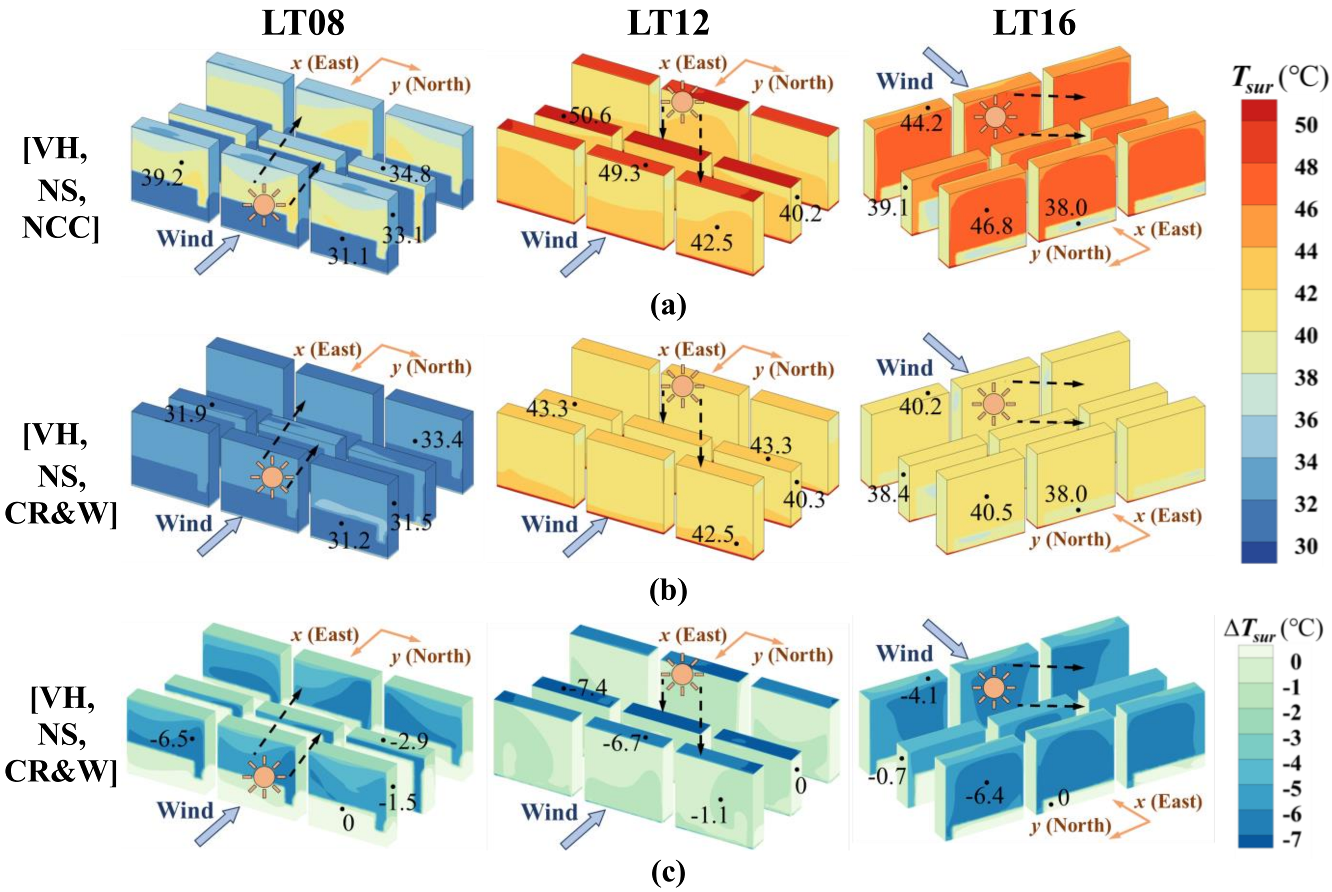

Fig. 7. Contour plots for the VH-NS model: building surface temperature (T_{sur}) under (a) NCC and (b) CR&W, and (c) the resultant building surface temperature drop (ΔT_{sur}) due to CR&W.

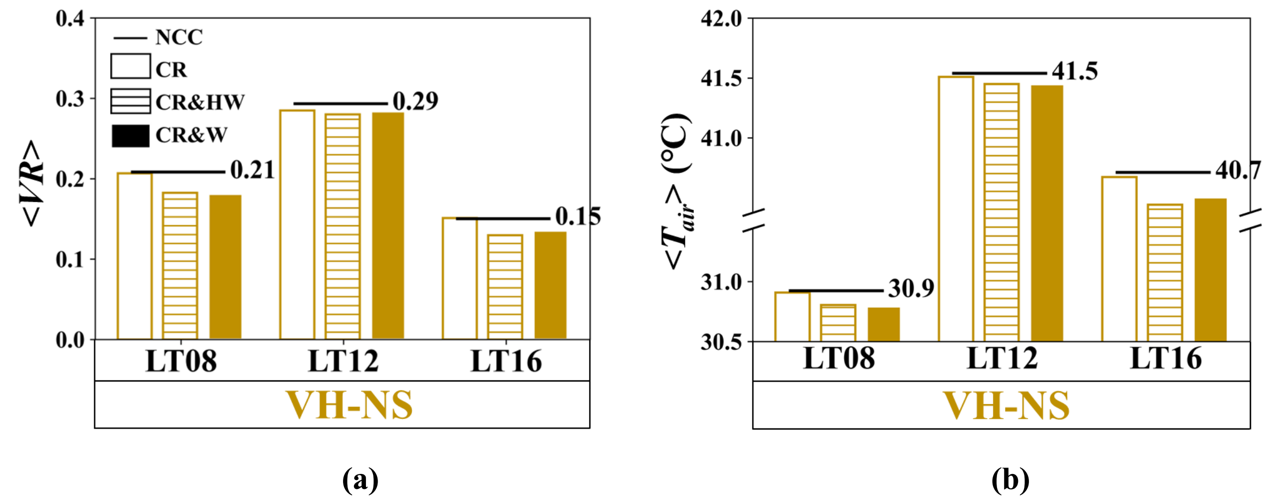

Fig. 8. Pedestrian-level area-averaged wind velocity ratio (<*VR*>) and air temperature (<T_{air}>) in the VH-NS model across different local times.

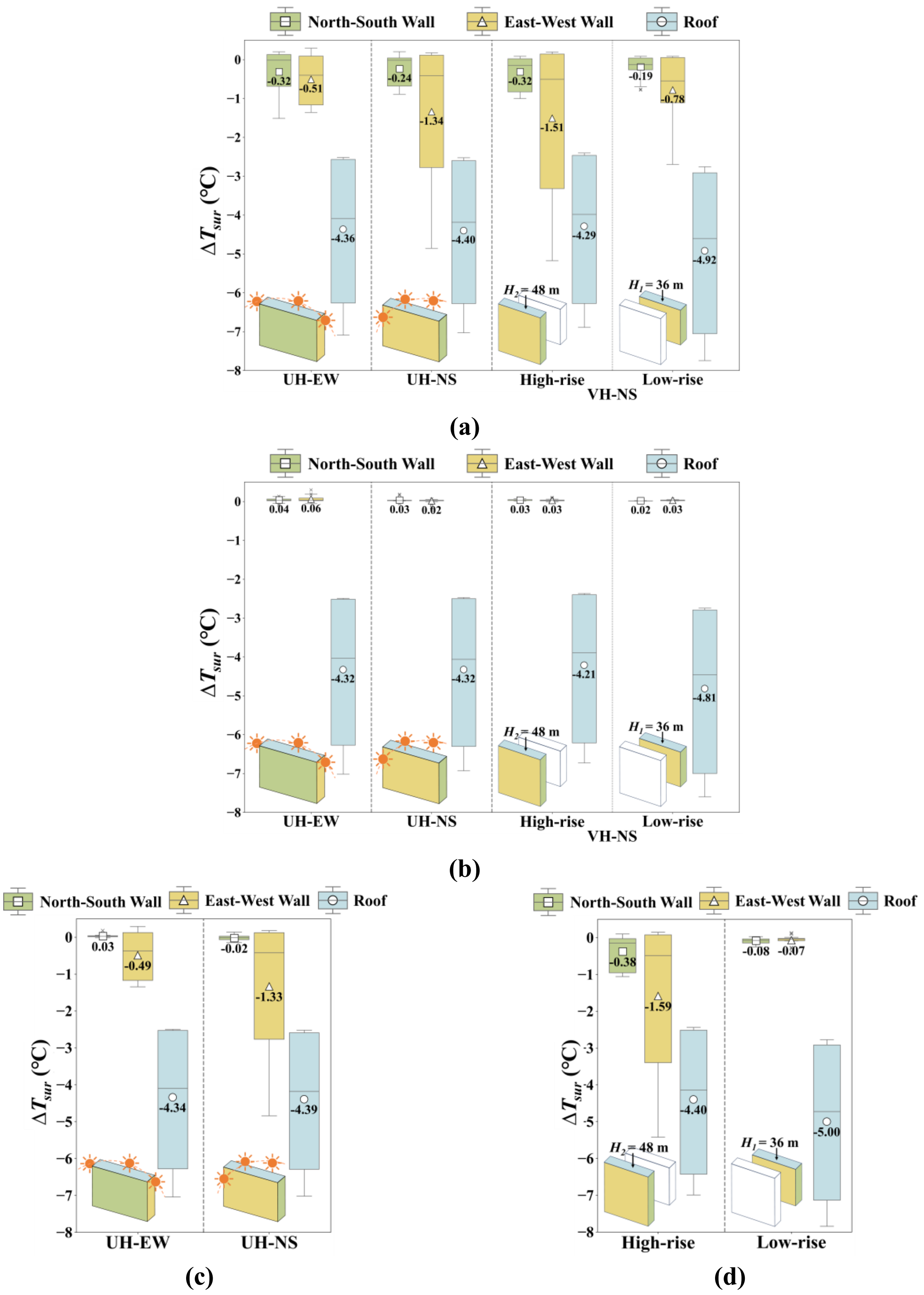

Fig. 9. Box plots of building surface temperature drop (ΔT_{sur}) on north-west walls, east-west walls, and roofs across different urban morphologies under (a) CR&W, (b) CR, (c) CR&EWW, and (d) CR&HW.

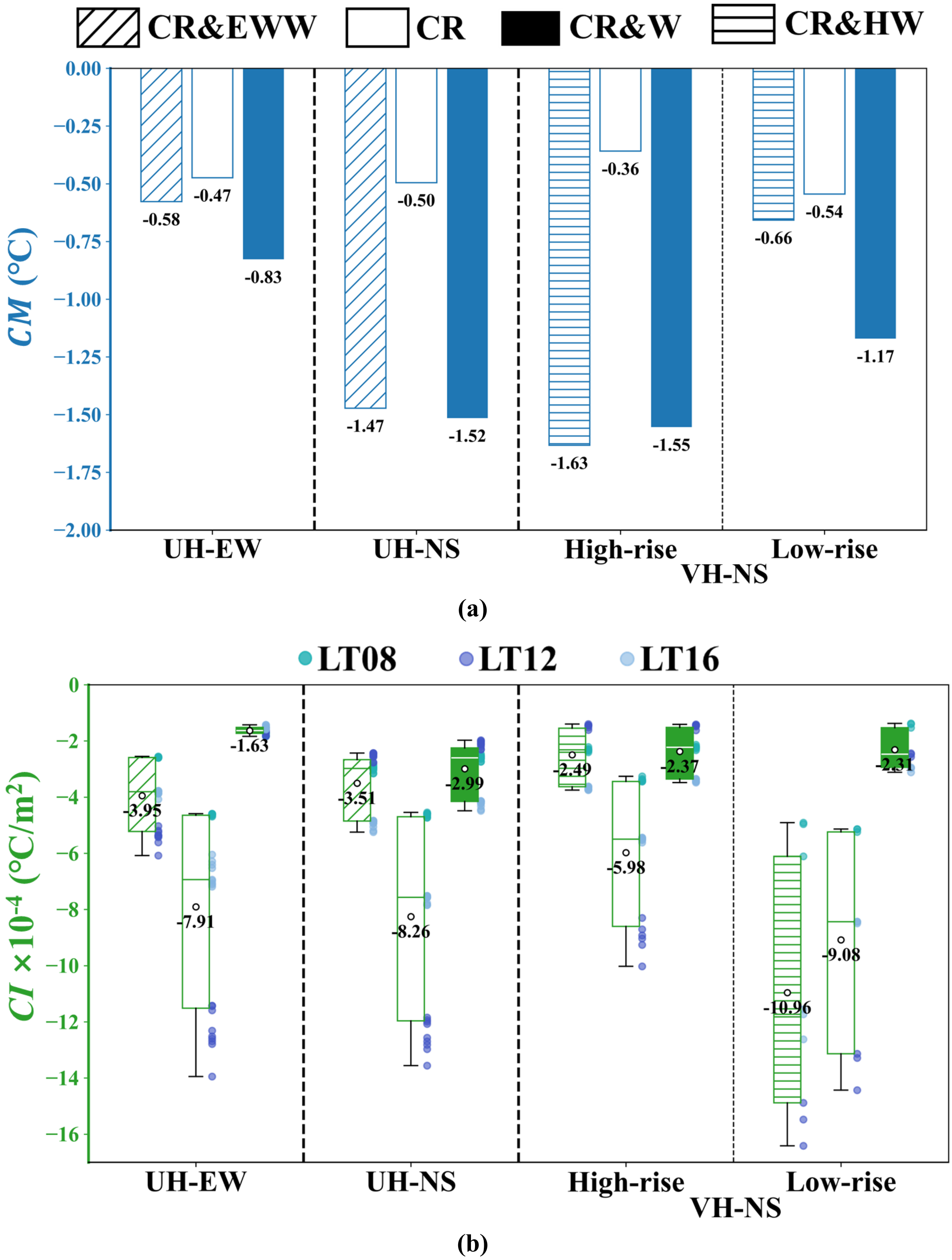

Fig. 10. Comparisons of (a) cooling magnitude (*CM*) and (b) cooling intensity (*CI*) induced by various cool coatings across different urban morphologies.

Table 1. Summary of studies on the impact of cool coatings on temperature and wind speed.

Reference	City/Climate	Model geometry	Coated surface	Impact of cool coating
Microscale numerical simulation				
Li et al. (2024)	Guangzhou, China Subtropical monsoon	2D idealized street canyon	CR, CW, CRW	Air cooling: < 0.2 °C; Surface cooling: up to 10.3 °C; Wind speed: nearly unchanged.
Xu et al. (2024c); Xu et al. (2023a)	Nanjing, China Subtropical monsoon	3D idealized building array	CRW	Surface cooling: up to 10.7 °C.
Donthu et al. (2024b)	Singapore Tropical rainforest	Real urban region	CR, CP, CW, CRW, CRP, CWP, CRWP	Air cooling: up to 2.8 °C; Surface cooling: up to 22 °C.
Elnabawi et al. (2023)	Al Ain, the UAE Tropical desert	Real urban region	CR	Air cooling: 0.49 °C (daytime), 0.34 °C (nighttime).
Zeeshan & Ali (2022)	Karachi, Pakistan Tropical monsoon	Real urban region	CRW, CP	Air cooling: < 0.3 °C; Surface cooling: up to 8 °C; Wind speed: increase by 0.5m/s.
Zhu et al. (2021)	Xi'an, China Temperate continental	Real urban region	CW, CR	Air cooling: < 0.1 °C; Surface cooling: 23–26 °C.
Sinsel et al. (2021b)	New York, the U.S. Temperate continental	3D idealized building array	CR	Air cooling: 0.7 °C (midday), 0.15 °C (nighttime).

Georgakis et al. (2014)	Athens, Greece Mediterranean	Real street canyon	CWP	Air cooling: < 1 ℃; Surface cooling: 2–3 ℃ (wall).
Experiment				
Hang et al. (2025); Lu et al. (2023)	Guangzhou, China Subtropical monsoon	Scaled-down 3D idealized building array	CR, CW, CRW	Air cooling: < 1 ℃; Surface cooling: up to 4.5 ℃ (wall), up to 10 ℃ (roof).
Xu et al. (2024b)	Nanjing, China Subtropical monsoon	Scaled-down 3D idealized building array	CR	Surface cooling: up to 9.2 ℃.
Donthu et al. (2024a)	Singapore Tropical rainforest	Real urban region	CRWP	Air cooling: up to 1 ℃; Surface cooling: up to 5.8 ℃ (wall), up to 25.2 ℃ (roof)
He et al. (2020)	Shanghai, China Subtropical monsoon	Scaled-down 3D idealized building array	CR	Surface cooling:14.5 ℃ (maximum), 3.3 ℃ (average).
Kolokotsa et al. (2018)	Attica, Greece Mediterranean	Real urban region	CR	Surface cooling: up to 10 ℃.
Mesoscale numerical simulation				
Wang et al. (2023)	Pearl River Delta, China Subtropical monsoon	Real urban region	CR	Air cooling: more than 1 ℃; Surface cooling: more than 2.5 ℃; Wind speed: decrease by over 0.4 m/s

Reed & Sun (2023)	Kansas, the U.S. Temperate continental	Real urban region	CR	Air cooling: 0.2–0.45 ℃; Surface cooling: 1.5–3.6 ℃.
Zhou et al. (2020)	Singapore Tropical rainforest	Real urban region	CR, CW, CP, CRW, CRP, CWP, CRWP	Air cooling: up to 3.1 ℃ (midday), up to 0.5 ℃ (nighttime); Surface cooling: up to 9.8 ℃.
Liu et al. (2020)	Sydney, Australia Subtropical monsoon	Real urban region	CRWP	Air cooling: 0.9 ℃ (maximum), 0.76 ℃ (average).
Zhang et al. (2019)	Los Angeles Basin, the U.S. Mediterranean	Real urban region	CR, CW	Air cooling: 0.45 ℃ (CR), 0.24 ℃ (CW); Wind speed: decrease by up to 0.21 (CR) and 0.08 (CW).
Cao et al. (2015)	Guangzhou, China Subtropical monsoon	Real urban region	CR	Air cooling: up to 1.2 ℃.

CR: Cool Roof; CW: Cool Wall; CP: Cool Pavement; CRW: Cool Roof and Wall; CRWP: Cool Roof, Wall, and Pavement; CRP: Cool Roof and Pavement; CWP: Cool Wall and Pavement

Table 2. Model description of simulated cases.

Building height layout	Street orientation	Cool coating configuration	Local time (LT)
Uniform Height (UH)	Long-side walls and	NCC	LT08
H = 36 m	wide streets extend		LT12
	east-west (E-W)		LT16
		CR&W	LT08
			LT12
			LT16
		CR	LT08
			LT12
			LT16
		CR&EWW	LT08
			LT12
			LT16
Uniform Height (UH)	Long-side walls and	NCC	LT08
H = 36 m	wide streets extend		LT12
	north-south (N-S)		LT16
		CR&W	LT08
			LT12
			LT16
		CR	LT08
			LT12
			LT16
		CR&EWW	LT08
			LT12
			LT16
Varied Height (VH)	Long-side walls and	NCC	LT08
H_1 = 36 m (low-rise),	wide streets extend		LT12
H_2 = 48 m (high-rise)	north-south (N-S)		LT16
		CR&W	LT08
			LT12
			LT16
		CR	LT08
			LT12
			LT16
		CR&HW	LT08
			LT12
			LT16

Table 3. Background temperatures, solar azimuths, and solar altitudes for three local times (NCEI, 2025). Note that background temperatures are ambient inflow temperatures used as model inlet conditions.

Local time	Background temperature (°C)	Solar azimuth (°)	Solar altitude (°)
LT08	29.9	76.82	27.63
LT12	39	100.23	82.36
LT16	40	278.77	42.23

Table 4. Specifications of materials used in CFD simulations (Hang et al., 2025; Toparlar et al., 2015).

Materials	Absorptivity		Emissivity	Density (kg/m^3)	Specific heat ($J{\cdot}kg^{-1}{\cdot}K^{-1}$)	Thermal conductivity ($W{\cdot}m^{-1}{\cdot}K^{-1}$)
	Direct Visible	Direct IR				
Uncoated concrete	0.76	0.76	0.87	2420	618.18	2.07
Cool coating	0.24	0.24	0.94			
Ground	0.6	0.6	0.9	1150	650	1.5

Table 5. Average grid convergence index for wind velocity (GCI_U) and air temperature (GCI_T) between mesh arrangements along different reference lines.

Mesh type	GCI_U			GCI_T		
	Line H1	Line V1	Line V2	Line H1	Line V1	Line V2
Medium-Fine	2.07%	-	1.27%	0.13%	0.13%	0.06%
Coarse-Fine	3.44%	-	2.15%	0.22%	0.30%	0.12%

Click here to access/download
Supplementary materials
Revised Supplementary Material.docx

Declaration of interests

☒The authors declare that they have no known competing financial interests or personal relationships that could have appeared to influence the work reported in this paper.

☐The authors declare the following financial interests/personal relationships which may be considered as potential competing interests: